Earth, Planets and Space

FULL PAPER Open Access

Thermochronology of hydrothermal alteration zones in the Kii Peninsula, southwest Japan: an attempt for detecting the thermal anomalies and implications to the regional exhumation history

Shigeru Sueoka[1*], Hideki Iwano[2], Tohru Danhara[2], Masakazu Niwa[1], Mizuho Kanno[1], Barry P. Kohn[3], Makoto Kawamura[1], Tatsunori Yokoyama[1], Saya Kagami[1], Yasuhiro Ogita[1] and Takafumi Hirata[4]

Abstract

Fluid-inclusion and thermochronometric analyses have been applied to hydrothermal alteration zones and their host rocks outcropping in the Hongu area of the Kii Peninsula, southwestern Japan in an attempt to detect thermal anomalies related to hydrothermal events and quantify the thermal effects on the host rocks. Hydrothermal events at ~ 150 °C and ~ 200 °C were identified by fluid-inclusion microthermometry of quartz veins in the alteration zones. For the host rocks and alteration zones, in the youngest population zircon yielded U–Pb dates ranging between ~ 74.7–59.2 Ma, fission-track dates of ~ 27.2–16.6 Ma, and (U–Th)/He single-grain dates of ~ 23.6–8.7 Ma. Apatite yielded pooled fission-track ages of ~ 14.9–9.0 Ma. The zircon U–Pb dates constrain the maximum depositional ages of the sedimentary samples. However, the fission-track and (U–Th)/He dates show no clear trend as a function of distance from the alteration zones. Hence, no thermal anomaly was detected in the surrounding host rocks based on the thermochronometric data patterns. The fission-track and (U–Th)/He dates are rather thought to record regional thermal and exhumation histories rather than a direct thermal imprint of fluid flow, probably because the duration of such activity was too short or because fluid flow occurred before regional cooling events and were later thermally overprinted. Apatite fission-track ages of ~ 10 Ma may reflect regional mountain uplift and exhumation related to the obduction of the SW Japan lithospheric sliver onto the Shikoku Basin, or the rapid subduction of the Philippine Sea slab associated with the clockwise rotation of the Southwest Japan Arc.

Keywords Thermochronology, Fluid inclusions, Hydrothermal alteration zones, Thermal anomaly, Kii Peninsula, SW Japan

*Correspondence:
Shigeru Sueoka
sueoka.shigeru@jaea.go.jp
Full list of author information is available at the end of the article

Graphical Abstract

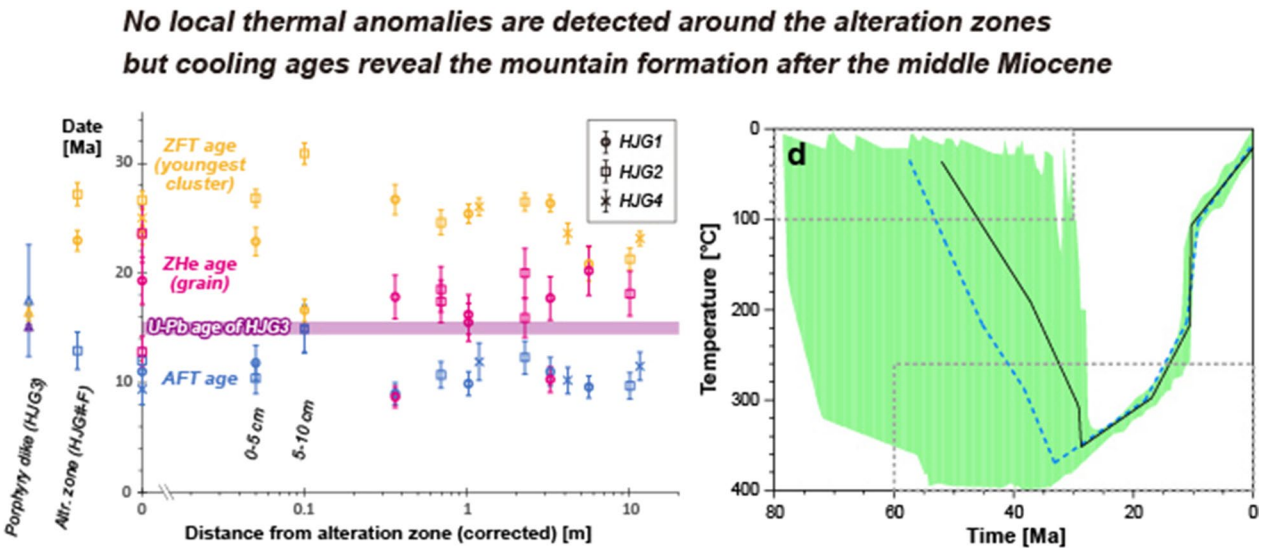

Introduction

Hydrothermal activity plays an important role in hydrological circulation, heat advection and element migration in the crust. Such activity can be related to magmatism, heat budget, crustal strength (Meissner and Wever 1992; Sibson and Rowland 2003), and the generation of earthquakes (Zhao et al. 1996; Obara 2002). In addition, it is also important for industrial and social demands related to the generation of ore deposits (Misra 2000; Cox 2005), development of geothermal resources (Bowen 2011), and evaluation for safety and stability of underground facilities (National Institute of Advanced Industrial Science and Technology 2016, 2017). Therefore, it is useful to develop techniques to detect evidence of hydrothermal activity and to evaluate the range of their effects.

Thermochronology can be used to constrain the thermal histories of rocks and minerals based on thermal resetting of radiometric ages. Since the 1970s, it has been applied to many geological events, such as, mountain building, basin development, and fault movement (e.g., Reiners et al. 2005; Ault et al. 2019; Malusá and Fitzgerald 2019a). Elucidating past hydrothermal activity is also an important target of thermochronology. For example, a growing number of studies have applied thermochronometry to detect thermal anomalies derived from fluid activity along fault zones (e.g., Tagami et al. 2001; Murakami et al. 2002; Tagami and Murakami 2007; Wölfler et al. 2010; Ault et al. 2016; Milesi et al. 2019, 2020; Louis et al. 2019; Sueoka et al. 2019; Jess et al. 2021). Furthermore, a number of studies have reported thermal anomalies and cooling dates related to ore-forming fluids (e.g., Arne et al. 1990; Wilson et al. 2003; Yuan et al. 2009; Márton et al. 2010; Wang et al. 2015). In all previous cases reported, the extent of the thermal anomalies typically ranged from 10^0 to 10^2 m or wider.

In this study, we attempt to detect local thermal anomalies around hydrothermal alteration zones by using a combination of geothermometry and multisystem thermochronology. An alteration zone is formed by paleo-fluid activity along a minor fault or crack. Such a minor fault or crack is expected to act as a temporal or relatively short-term pathway for fluids, in contrast to a major fault zone which is a stable and long-term pathway along which fluid activity over multiple pulses is often recorded (e.g., Tanaka et al. 2007), and a wide range of thermal anomalies are detected (e.g., Tagami et al. 2001; Murakami et al. 2002). However, hot springs are not always distributed along major fault zones (e.g., Kimbara 2005; Tamburello et al. 2022). Therefore, minor faults and cracks can be important factors that control crustal permeability. Hence, thermal anomalies along alteration zones, namely, fossils of paleo-fluid activity along minor faults and cracks, can provide clues for assessing the stability of individual fluid pathways and understanding the macro-permeability of the crust.

We investigated outcrops of hydrothermal alteration zones in the Hongu area of the Kii Peninsula, southwest Japan, where non-volcanic thermal fluid activity has been reported (e.g., Matsumoto et al. 2003; Umeda et al. 2006; Yamaguchi et al. 2009; Morikawa et al. 2016). The Kii

Peninsula contains no Quaternary volcanoes, thus providing a preferable area for studying the thermal effects of hydrothermal events without possible thermal disturbances caused by recent volcanism. The homogenization temperatures of the fluid inclusions (e.g., Roedder 1984) in the quartz veins of the alteration zones were measured to estimate the temperatures of the thermal fluids that formed the alteration zones. We also applied thermochronometric methods to the host rock enclosing the alteration zones in an attempt to constrain the timing, duration and spatial range of thermal-fluid activity. These methods include apatite and zircon fission-track (hereinafter called AFT and ZFT), zircon (U–Th)/He (hereinafter called ZHe), and zircon U–Pb analyses. Apatite (U–Th)/He (hereinafter called AHe) method was not adopted because the apatite grains, being generally small and non-euhedral, were not suitable for analysis. Using thermochronometry data, we also discuss the thermal and exhumation histories of accretionary complexes in the study area.

Geological setting

The Kii Peninsula is located in the Outer Zone of the Southwest Japan Arc, on the forearc side of the Median Tectonic Line (Fig. 1a). The Kii Peninsula features a number of high-temperature hot springs in the Shirahama, Katsu'ura, Ryujin, Tosenji, Totsukawa, and Hongu areas, although they are a few hundred kilometers away from the volcanic front of the Southwest Japan Arc (Fig. 1b). Various geochemical and geophysical studies support the finding that the high-temperature fluids in the Kii Peninsula originate from the Philippine Sea slab beneath this region. For example, $^{3}He/^{4}He$ ratios as high as ~ 4–5 R_A (Matsumoto et al. 2003; Umeda et al. 2006, 2007; Morikawa et al. 2016; 1 R_A = atmospheric $^{3}He/^{4}He$ ratio) and high Li/Cl ratios by weight (> 0.001) (Kazahaya et al. 2014) indicate that the groundwater contains deep-seated fluids. Seismicity, including seismic swarms (Kato et al. 2014) and deep low-frequency tremors (Obara 2002), supports fluid migration in the crust beneath the Kii Peninsula, and low resistivity (< 10 Ωm) between the Conrad discontinuity and the slab surface (Yamaguchi et al. 2009) suggests upward migration of fluid from the subducting slab.

The Kii Peninsula is composed predominantly of the Cretaceous to Miocene accretionary complexes of the Shimanto Belt and Miocene silicic rocks. The rocks of the Shimanto Belt have been roughly divided into the Cretaceous Hidakagawa, the Eocene Otonashigawa, and the Oligocene to early Miocene Muro Groups from the back-arc to forearc sides (Tokuoka et al. 1981) (Fig. 1b). In the Hongu area, the Haroku Formation of the Otonashigawa Group consists mainly of alternating sandstones and mudstones (Tokuoka et al. 1981). The Haroku Formation yielded Eocene radiolarian fossils (Suzuki 1993), and detrital zircons from the tuffaceous sandstone yielded U–Pb ages showing the youngest population of 50.8 ± 1.0 Ma (Tokiwa et al. 2016). Illite crystallinity values of 0.54 and 0.64 Δ°2θ were obtained from the northern area of the Otonashigawa Group in the western Kii Peninsula, which were converted into paleo-temperatures of ~ 227 °C and ~ 192 °C with an error of at least 50 °C using the calibration of Underwood et al. (1993) (Awan and Kimura 1996). For the Hidakagawa Group to the north of the Otonashigawa Group (Fig. 1b), the paleo-temperatures of ~ 310 °C and ~ 250 °C were similarly obtained in the northern and southern parts, as well as the pressures of ~ 3.6 kbar and ~ 2.2 kbar (equivalent to the burial depths of ~ 14 km and ~ 8 km) based on the illite b_0 lattice spacing values (Awan and Kimura 1996). Considering the southward lowering trend of the paleo-temperatures, the burial depth of the Otonashigawa Group is thought to have been shallower than ~ 8 km.

ZFT and AFT thermochronology have been reported in previous studies that investigated the thermal and exhumation history of the accretionary complexes of the Shimanto Belt on the Kii Peninsula (e.g., Tagami et al. 1995; Hasebe and Tagami 2001; Hasebe and Watanabe 2004; Umeda et al. 2007; Hanamuro et al. 2008; Ohira et al. 2016), as well as in other regions of the Southwest Japan Arc (Hasebe et al. 1993b, 1997) (Fig. 2). On eastern Shikoku Island, the maximum temperature during accretion varied regionally. Cretaceous rocks of the Northern Shimanto Belt were heated to the partial annealing zone (PAZ; see Sect. "Strategies" for more details) of ZFT system, yielding grain ages younger than the depositional ages. However, the grains in the rocks of the Southern Shimanto Belt are older than the Eocene–Miocene time of deposition, and as such, have not been heated

(See figure on next page.)

Fig. 1 Map of study area. **a** Tectonic and hydrological settings of the Southwest Japan Arc. Data for Quaternary volcanoes and hot springs are sourced from the Committee for Catalog of Quaternary Volcanoes in Japan (1999) and Kimbara (2005), respectively. Gray contours denote the depth of the upper surface of PHS slab at 10-km intervals (Nakajima and Hasegawa 2007; Hirose et al. 2008a, b; Nakajima et al. 2009); **b** Geologic map of the Kii Peninsula, outlined by the red square in (**a**) above, modified after Wakita et al. (2009), showing active fault traces (Nakata and Imaizumi 2002) and hot springs (Kimbara 2005). [MTL, Median Tectonic Line; NE, Northeast; PAC, Pacific plate; PHS, Philippine Sea plate; SW, Southwest]

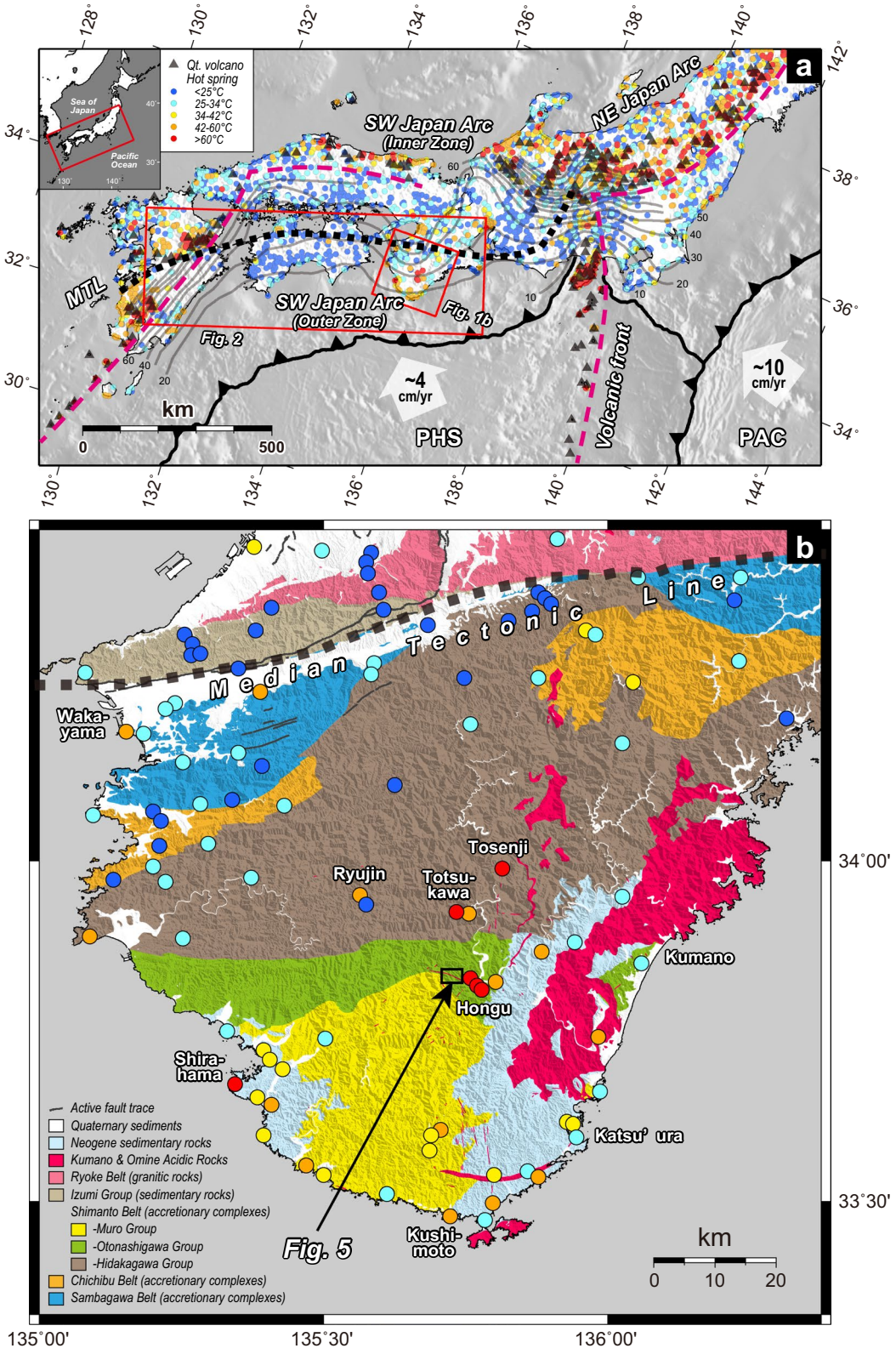

Fig. 1 (See legend on previous page.)

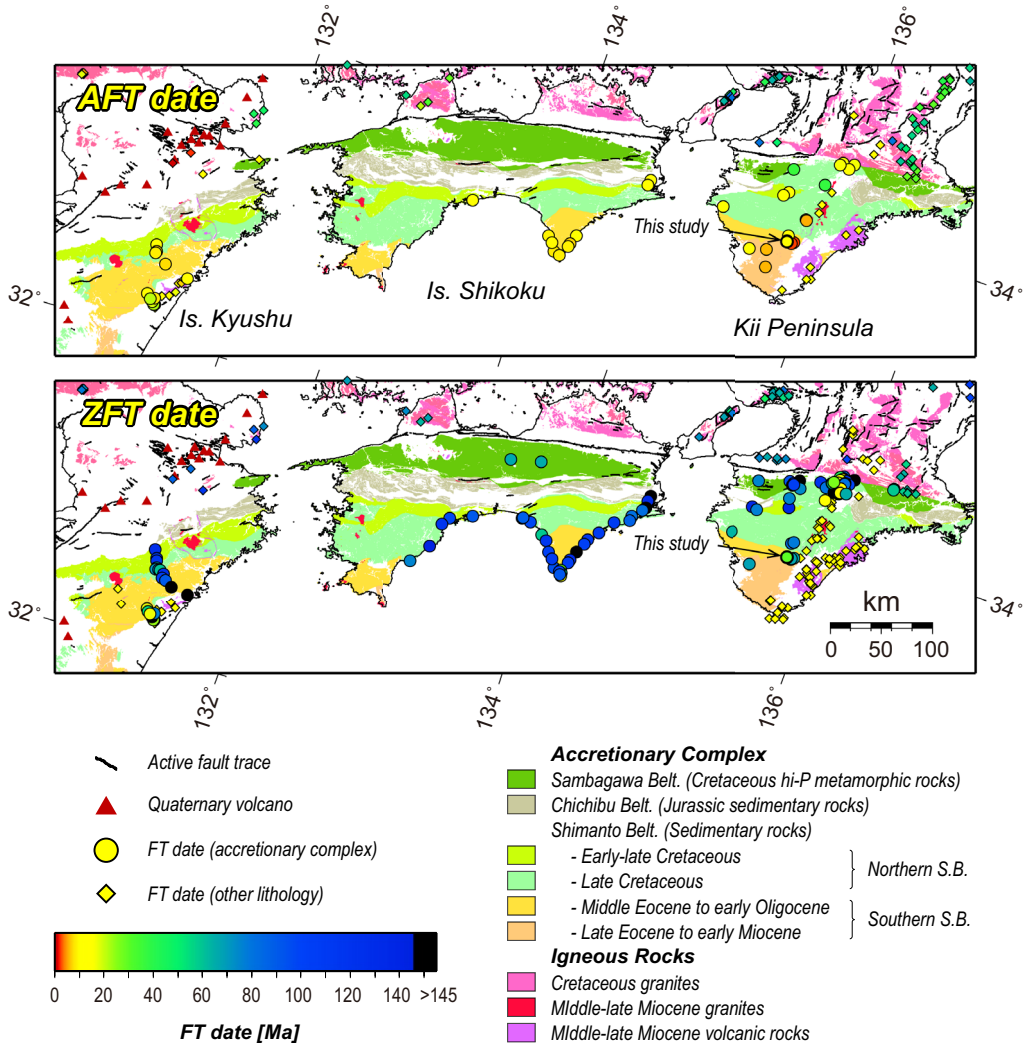

Fig. 2 Fission-track ages in Shimanto Belt on the forearc side of the Southwest Japan Arc. Age data were obtained from the low-temperature thermochronological database v.1.05.00 (Sueoka and Tagami 2019) and references therein. The pooled FT ages of 19 sedimentary and alteration-zone samples from this study are plotted at location HJG1 on the map; although the central age was adopted for zircon in the main text, the pooled age of all the grains is shown here for comparison with the reported ZFT dates. The geologic map was modified after Wakita et al. (2009). Active fault traces and Quaternary volcanoes are from Nakata and Imaizumi (2002) and Committee for Catalog of Quaternary Volcanoes in Japan (1999). [hi-P, high-pressure; S.B., Shimanto Belt]

to temperatures in the ZFT PAZ (Hasebe et al. 1993b; Tagami et al. 1995). In contrast, AFT ages of ~ 10 Ma were obtained in both the Northern and Southern Shimanto Belts. These AFT ages are significantly younger than the deposition ages, reflecting a rapid cooling and exhumation episode straddling the AFT PAZ at ~ 10 Ma (Hasebe et al. 1993b). Fission-track data in western Shikoku Island and Kyushu Island indicate similar thermal histories, except for local reheating episodes, such as the granitic intrusion at ~ 15 Ma (Tagami and Shimada 1996; Hasebe et al. 1997; Hasebe and Tagami 2001). Fission-track data for the Kii Peninsula are also largely consistent with other regions, but differ in the following points: (1) AFT ages young southward from ~ 35 Ma to ~ 13 Ma in the Northern Shimanto Belt and ~ 6 Ma in the Southern Shimanto Belt (Hasebe and Tagami 2001); (2) young AFT ages (~ 5–2.5 Ma) near hot springs have been reported (Umeda et al. 2007; Hanamuro et al. 2008); (3) a patchy age distribution of Miocene ZFT ages is likely related to heat influx (Hasebe and Watanabe 2004); and (4) accretion-related heating to the upper limit of the ZFT PAZ has been determined for some regions of the Northern Shimanto Belt (Ohira et al. 2016).

Miocene silicic rocks in the Kii Peninsula have been divided into the Kumano Acidic Rocks and Omine Acidic Rocks. The Kumano Acidic Rocks were generally formed by igneous activity of the Kumano Caldera (Miura 1999; Kawakami et al. 2007), with some exceptions. For example, the Konogi Rhyolite, forming the lower part of the Kumano Acidic Rocks, was produced by subaerial eruptions from fissures preceding the main eruption from the Kumano Caldera (Aramaki 1965). The lithologic units of the Kumano rocks consist of granite, granite porphyry, and pyroclastic breccia found within the accretionary complex of the Shimanto Belt (Miura 1999). The Omine rocks are distributed in several separate units and are composed mainly of granodiorite, granite, and granite porphyry (Kawasaki 1980). The arcuate and semicircular dike swarms of the Omine rocks in the central part of the Kii Mountains are thought to have been formed in association with the formation/collapse of the Omine and Odai Cauldrons, respectively (Sato and Yamato Omine Research Group 2006), although many of the plutonic stocks of the Omine rocks are apparently not associated with these cauldrons. Radiometric ages for the Kumano Acidic Rocks and Omine Acidic Rocks are generally in the range of ~ 16–14 Ma, as estimated by various methods, including AFT and ZFT (Hasebe et al. 1993a, 2000; Iwano et al. 2007, 2009) (Fig. 2), biotite K–Ar (Sumii et al. 1998; Sumii and Shinjoe 2003), and zircon U–Pb (Orihashi et al. 2007), suggesting that their formation and rapid post-emplacement cooling occurred during the middle Miocene.

Methodology

Strategies

To detect and evaluate thermal anomalies around hydrothermal alteration zones, we adopted an approach that combined geothermometric data from hydrothermal alteration zones with thermochronometric information from their host rocks (Fig. 3). Cooling ages of a thermochronometer reflect the thermal histories around their typical closure temperatures: ~ 50 °C–80 °C for AHe (Farley 2000; Flowers et al. 2009), ~ 90 °C–120 °C for AFT (Ketcham et al. 1999, 2007), ~ 160 °C–200 °C for ZHe (Reiners et al. 2004; Guenthner et al. 2013), ~ 300 °C for ZFT (Yamada et al. 2007; Ketcham 2019), and > ~ 900 °C for zircon U–Pb systems (Cherniak and Watson 2000) for cooling on geological timescales (e.g., 1–100 °C/Myr) and under typical mineralogical conditions (e.g., euhedral, ~ 60–150-μm-wide, low radiation-damage, and general chemical compositional grains). Cooling ages are partially reset in a temperature zone around the closure temperature, called the partial annealing zone (PAZ) or partial retention zone (PRZ). The cooling ages are totally reset above the PAZ (or PRZ) and not reset below it.

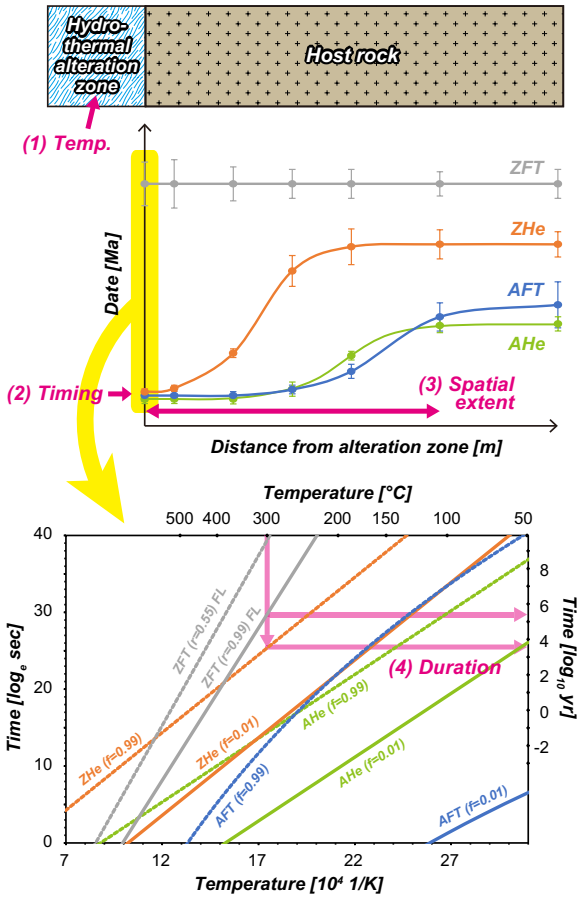

Fig. 3 Schematic plots showing basic concepts of sampling and analytical strategies. (1) Fluid temperatures are estimated from the alteration zones using geothermometers. (2) The timings of fluid activity can be equivalent to the cooling ages of the host rocks nearest to the alteration zones if the ages are totally reset by heating. (3) The spatial pattern of the thermal effects of fluid activity is constrained by thermochronometric data obtained from host rocks at various distances from the alteration zones. Regional cooling and exhumation histories are reconstructed from the undisturbed host rocks at a certain distance from the alteration zones. (4) The duration of fluid activity can be constrained by comparing thermochronometric data from the host rocks nearest to the alteration zones. If a thermochronometric system is totally reset and another is not, the heating duration can be constrained by the kinetics of those systems and the temperatures estimated in (1). Plots denote fractional-loss contours of ZFT, ZHe, AFT, and AHe systems constructed after Yamada et al. (2007) and Reiners (2009), respectively. [f, fractional loss; FL, Fanning linear model; *r*, reduced fission-track lengths]

When partially or not reset, the cooling ages are affected by thermal histories prior to the last heating episode. For example, igneous rocks can reflect initial cooling immediately after their intrusion, whereas sedimentary rocks and detrital samples may record thermal/exhumation histories in the provenance areas (Malusá and Fitzgerald 2020).

Kinetic models for thermochronometers (i.e., the relationship between cooling ages and time–temperature conditions) are described by linear or curvilinear functions in Arrhenius space where the ordinate axis represents logarithmic time and the abscissa axis represents reciprocal temperature (e.g., Reiners 2009). In other words, the thermal resetting of samples depends predominantly on the heating duration and temperature. Although the PAZ or PRZ over 10^6–10^7 years are generally used for geological events, the duration of crustal fluid activity is expected to be considerably shorter (Beinlich et al. 2020; Mukuhira et al. 2022). In this study, we determine paleotemperatures using an independent geothermometer, and the heating duration is derived from thermochronological data (Fig. 3).

The temperature of the fossil fluid activity is initially determined by applying geothermometry to vein samples obtained from the alteration zones, and the timing of the activity is estimated based on the cooling ages of the host rocks near the alteration zone. This strategy assumes that fluids were sufficiently hot to totally reset some cooling ages, and that the thermal anomalies were related to heat conduction rather than to fluid migration in the host rocks. The spatial extent of thermal effects can be constrained using multiple thermochronometric methods with different temperature sensitivities, applied at progressive distances from the hydrothermal alteration zones. The duration of thermal-fluid activity can be computed by comparing different datasets acquired from the alteration zones and host rock samples. Because fluid temperatures are determined by geothermometry, the duration of activity can also be constrained using kinetic models of thermochronometers if the cooling age of the host rock is reset by hydrothermal activity. For example, if the cooling age of a thermochronometer is totally reset (or not reset at all), the minimum (or maximum) duration can be determined from the upper (or lower) limit of the PAZ or PRZ. By combining multiple thermochronometers with various kinetic properties, the duration can be constrained even more precisely when some thermochronometric systems are totally reset and others are not. In cases of partial resetting, instead of total (or not) resetting, the minimum (or maximum) duration is loosely constrained between the upper and lower limits of the PAZ or PRZ.

Model prediction

Thermal modeling was performed to predict the ranges within which the cooling ages were reset by fluid activity in a general and simple situation. A simple 1-D heat conduction was assumed here; advection of the fluid was not incorporated; therefore, the computed results provided minimal ranges of thermal anomalies. The calculation was based on the following equation:

$$\frac{\partial^2 T}{\partial x^2} = \frac{1}{a}\frac{\partial T}{\partial t}$$

where T is the temperature (°C), x is the horizontal distance (m), a is the thermal diffusivity ($=2.10\times10^{-6}$ m^2/s), and t is time (s). Fluid activity occurred at $x=0$, and the temperature changes in the host rocks at $x>0$ were simulated. The temperature of the fluid (T_f) was given by four patterns (150, 200, 250, and 300 °C) and was set temporarily constant. The initial temperature (T_0) of the host rocks was set as 20 °C. The duration of fluid activity (t_f) was up to 1000 years.

The temperature changes at each location were converted into thermochronometric ages. The calculations were performed based on the forward model of HeFTy ver.1.9.3 (Ketcham 2005) with the following kinetic models: AHe system, Flowers et al. (2009); AFT system, Ketcham et al. (2007); ZHe system, Guenthner et al. (2013); ZFT system, the fanning Arrhenius model of Yamada et al. (2007). For simplification, the host rocks were situated at 20 °C since 50 Ma, and fluid activity started at 10 Ma. If not disturbed by fluid activity, the cooling dates of any thermochronometric system are predicted to be 50 Ma at any location. When comparing the modeling results with natural data, these values should be replaced by more robust values in each study area, considering the expected depth and timing of the fluid activity and cooling ages of the thermally undisturbed host rocks.

The modeling results are shown in Fig. 4. Based on the results, the following age patterns are expected: no system yields significantly younger ages for $T_f=150$ °C and $t_f<1000$ year, except for the AHe system for $t_f=1000$ year; the AHe, AFT, and ZHe systems can yield younger ages for $T_f>200$ °C depending on x and t_f, and the ZFT system does not yield significantly younger ages for $T_f<300$ °C and $t_f<1000$ year. It is likely that t_f needs to be longer than 10^6 years for $T_f<300$ °C to make the ZFT ages younger because the lower limit of the ZFT PAZ is ~ 250–300 °C for 10^6 years of isothermal heating (Yamada et al. 2007). It is noteworthy that the AHe system sometimes produces dates older than those of the AFT system for high-temperature short-term heating (i.e., 250 °C for 0.1–10 years and 300 °C for 0.1–1 years), as predicted by Reiners (2009). It is also notable that an age discrepancy is not obvious between $x=0.01$ m and 0.3 m, indicating that precise sampling on a few cm scale is not required to detect thermal anomalies by fluid activities in such a setting. This observation contrasts with the cases of frictional heating along a fault zone (e.g., d'Alessio et al. 2003; Murakami and Tagami 2004) and wildfire heating (Mitchell and Reiners 2003; Reiners et al. 2007),

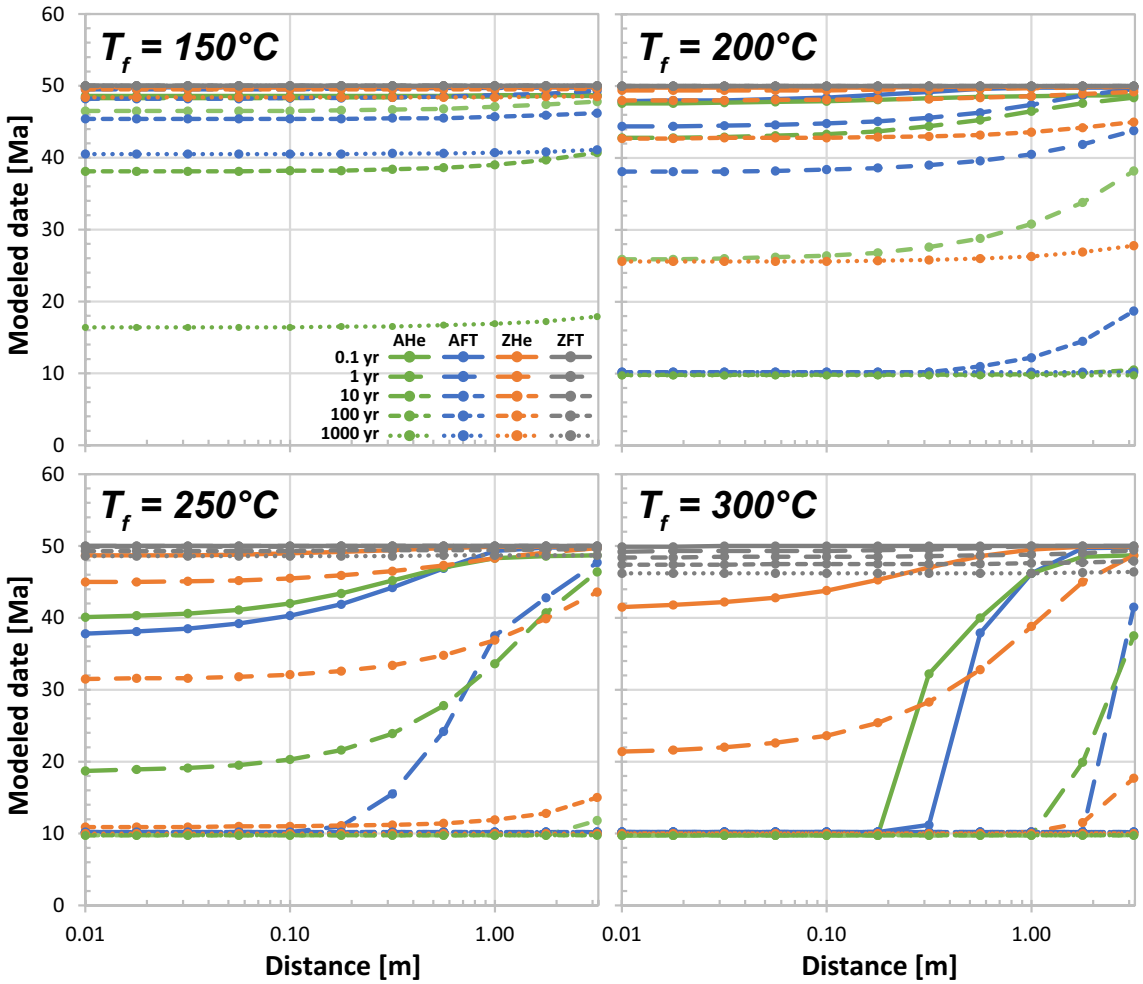

Fig. 4 Predicted patterns of thermochronometric ages. Rocks are assumed to have been located at 20 °C since 50 Ma and then heated by thermal conduction derived from the hydrothermal activity of a constant fluid temperature, T_f, occurring at $x = 0$ m since 10 Ma

for which sampling at the millimeter or centimeter scale is necessary. This contrast must be derived from the difference in the heating duration (Tagami 2019).

Sample collection

To follow the strategies outlined in Sects. "Strategies" and "Model prediction", hydrothermal alteration zones and their host rocks were sampled from three locations (HJG1, HJG 2, and HJG4) in the Hongu area in the central part of the Kii Peninsula (Fig. 5). In these outcrops, hydrothermal alteration zones of ~ 0.5-m width, accompanied by nested hydrothermal veins, are exposed in the sandstone and mudstone of the Haroku Formation. These zones include abundant quartz, epidote, chlorite, and sulfide minerals, such as pyrite, pyrrhotite, and chalcopyrite. Widespread brown, friable deposits composed mainly of goethite fill the gaps on the alteration surfaces. The vein quartz commonly exhibits holocrystalline, hypidiomorphic and blocky textures, which are easily distinguished from fragmented quartz in the host rocks (Fig. 6). The host-rock Haroku Formation typically shows alternating beds of ~ 10–50-cm-thick sandstones with some interbedded ~ 1-cm-thick mudstones. Although these beds are often folded and have variable strikes, they mostly exhibit gentle dips. In contrast, the near-vertical alteration zones cut the bedding of the Haroku Formation, penetrating both the sandstone and mudstone.

At each outcrop, one sample was collected from the alteration zone for fluid-inclusion analysis and thermochronometry, and several samples were collected from the host sandstones for thermochronometry (fission-track (FT), (U–Th)/He, and U–Pb analyses) (Table 1, Fig. 5). ~ 20–30-cm-wide sandstone samples were collected using a hammer and chisel at distances of ~ 0 m, ~ 0.3 m, ~ 1 m, ~ 10 m, and ~ 20 m from the margin of the alteration zones. The distances were measured

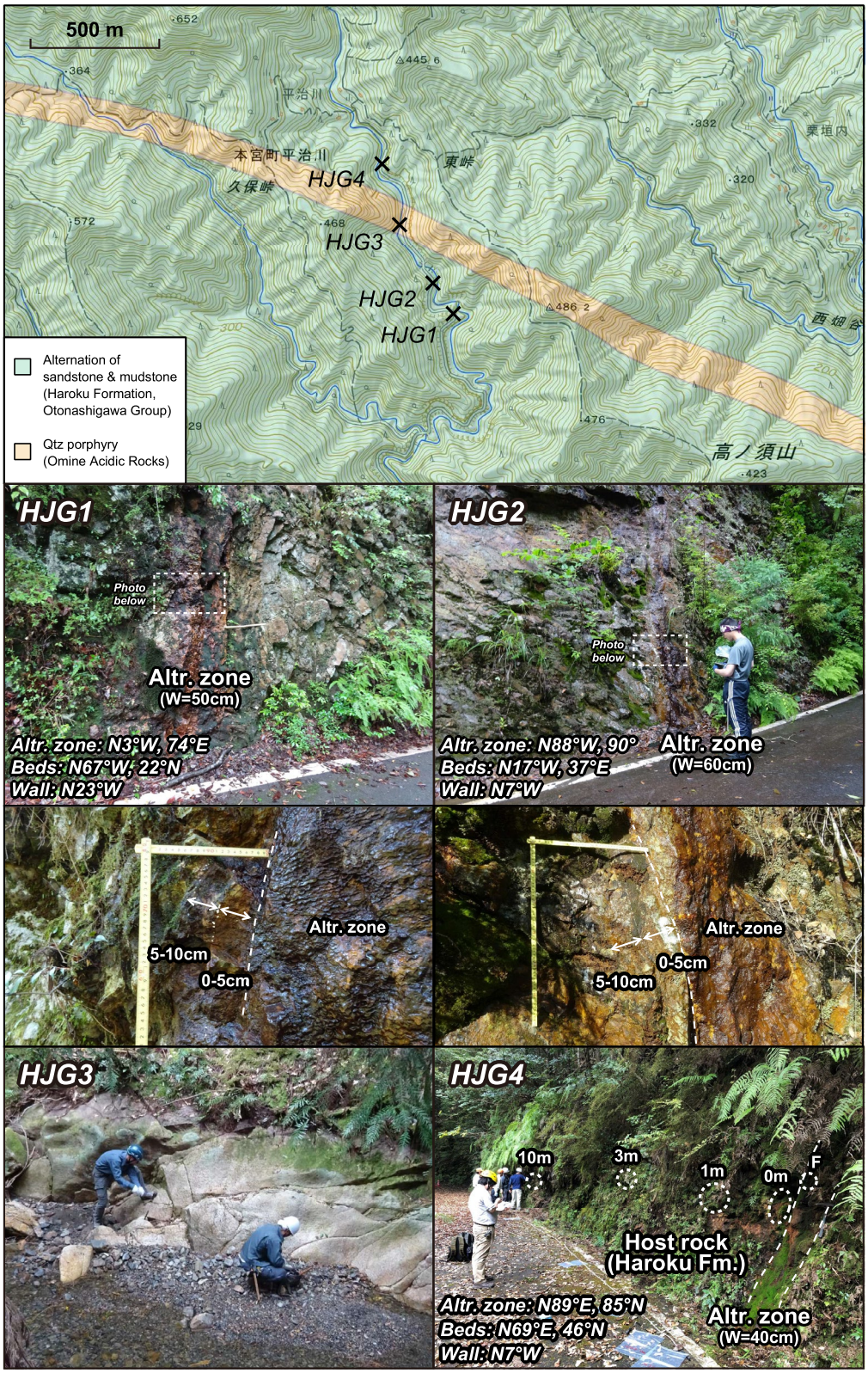

Fig. 5 Sample localities and outcrop photographs. Map based on geological map of Wakita et al. (2009) and GSI Maps from Geospatial Information Authority of Japan. The strikes incorporate a declination correction of ~ 7°W. Field photos show alteration zones and specific sampling locations (HJG1, HJG2, HJG3, and HJG4). Dashed circles or ellipses in the HJG4 photograph show the specific sample sites for HJG4-F, - 0 m, - 1 m, - 3 m, and - 10 m. [Fm., Formation; Qtz, quartz; W, width]

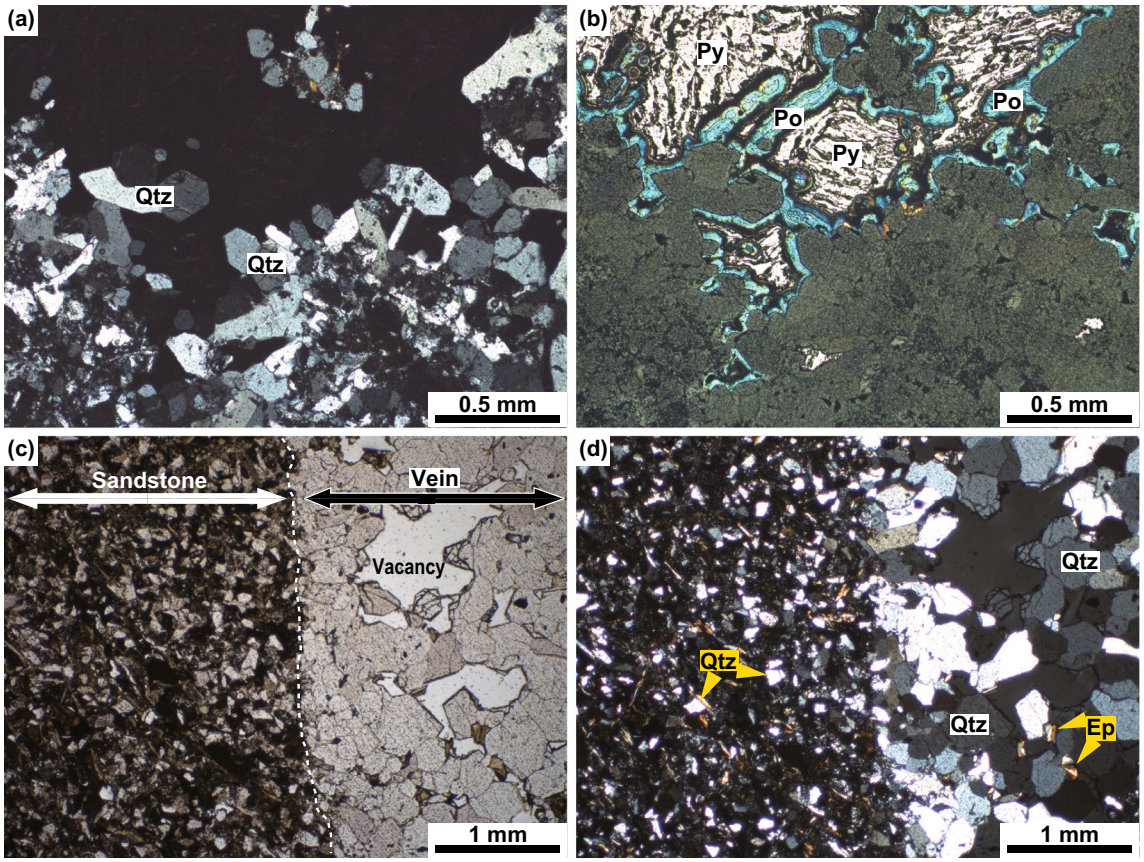

Fig. 6 Photomicrographs of vein rocks from the alteration zone of HJG1. **a**, **b** Quartz in blocky-textured vein rock under cross-polarized and reflected light; **c**, **d** veins cutting through sandstone under plane-polarized and cross-polarized light; quartz is holocrystalline and hypidiomorphic in veins but fragmented in sandstone. [Ep, epidote; Po, pyrrhotite; Py, pyrite; Qtz, quartz]

horizontally along the outcrop walls and then converted into three-dimensional distances based on strike and dip measurements of the margins. In addition, ~ 5 cm thick sandstones were obtained using a hand grinder at a distance of 0–5 cm and 5–10 cm from the margin, in order to detect minor thermal anomalies near the alteration zones. The thicknesses were precisely measured perpendicular to the margin.

Because the intrusive rocks outcrop at location HJG3 (near locations HJG1, HJG2, and HJG4), a sample was obtained for zircon U–Pb analysis, which could potentially be helpful in assessing whether the cooling ages at locations HJG1, HJG2, and HJG4 reflect thermal effects related to the intrusion rather than from hydrothermal activity. The intrusive rock, which belongs to the Omine unit, consists of coarse ($\phi = \sim 5$–8 mm) quartz porphyry containing brownish altered feldspars and mafic minerals. The northern contact between this intrusive body and the Haroku Formation is sharp and strikes at N57°W, 82°N. According to the geological map, the distance from the sample locations in the Haroku Formation to the margin of the intrusive body was ~ 200 m for HJG1 and ~ 100 m for HJG2 and HJG4.

Analyses applied

Geothermometric measurements using fluid-inclusion data were performed on three samples collected from quartz veins of the alteration zones to estimate the temperatures of the geothermal activity that formed the alteration zones. The homogenization temperatures and final ice-melting temperatures were measured at the Geothermal Engineering Co., Ltd. (Additional file 1: Text S1). Geo- and thermochronological analyses using the ZHe, AFT, ZFT, and U–Pb zircon methods were performed on 17 host-rock samples and two alteration zone samples (Table 1). Mineral separations, FT dating, FT length measurements, and U–Pb dating were conducted mainly at the Kyoto Fission-Track Co., Ltd. (Additional file 1: Text S2, Additional file 8: Table S1). U–Pb dating of the intrusive rock sample was performed at the Tono Geoscience Center, Japan Atomic Energy Agency (Additional file 1: Text S2, Additional file 9: Table S2). Helium

Table 1 List of samples

Sample code	Lithology	L [m]	Corr. L [m]	Analysis performed			
				Fluid inclusion	U–Pb	FT	(U-Th)/He
Loc. HJG1 (N33°49′ 52.64″, E135°43′ 26.47″)							
HJG1-F	Alteration zone	–	–	Y	Y	Y	–
HJG1-0–5 cm	Sandstone	–	0.00–0.05	–	Y	Y	–
HJG1-5–10 cm	Sandstone	–	0.05–0.10	–	Y	Y	–
HJG1-0 m	Sandstone	0.0	0.0	–	Y	Y	Y
HJG1-1 m	Sandstone	1.1	0.4	–	Y	Y	Y
HJG1-3 m	Sandstone	3.1	1.0	–	Y	Y	Y
HJG1-10 m	Sandstone	9.9	3.3	–	Y	Y	Y
HJG1-20 m	Sandstone	17.1	5.6	–	Y	Y	Y
Loc. HJG2 (N33°49′ 56.04″, E135°43′ 23.75″)							
HJG2-F	Alteration zone	–	–	Y	Y	Y	-
HJG2-0–5 cm	Sandstone	–	0.00–0.05	–	Y	Y	-
HJG2-5–10 cm	Sandstone	–	0.05–0.10	–	Y	Y	-
HJG2-0 m	Sandstone	0.0	0.0	–	Y	Y	Y
HJG2-1 m	Sandstone	0.7	0.7	–	Y	Y	Y
HJG2-3 m	Sandstone	2.3	2.3	–	Y	Y	Y
HJG2-10 m	Sandstone	10.2	10.1	–	Y	Y	Y
Loc. HJG3 (N33°50′ 02.84″, E135°43′ 18.79″)							
HJG3-Upb	Qtz porphyry	–	–	–	Y	Y	–
Loc. HJG4 (N33°50′ 10.26″, E135°43′ 15.27″)							
HJG4-F	Alteration zone	–	–	Y	–	–	–
HJG4-0 m	Sandstone	0.0	0.0	–	Y	Y	–
HJG4-1 m	Sandstone	1.2	1.2	–	Y	Y	–
HJG4-3 m	Sandstone	4.2	4.2	–	Y	Y	–
HJG4-10 m	Sandstone	11.7	11.6	–	Y	Y	–

The latitude and longitude of the sample localities were obtained using a handheld GPS and are shown in WGS84. L indicates the horizontal distance from the alteration zones along the outcrop surfaces and Corr. L denotes the horizontal distance from the alteration zones calibrated against the strikes/dips of the alteration zones and the strikes of the outcrop walls (Fig. 5). Note that the uncertainties for L. and Corr. L of HJG#-#m are typically ± 10–15 cm, reflecting the width of the rock samples, whereas those of HJG#-#-#cm are < 1 cm. [Loc., locality; Qtz, quartz; Y, yes (analysis performed on sample)]

measurements using an Alphachron system for (U–Th)/He dating were performed at the Tono Geoscience Center (Additional file 1: Text S3). The U–Th content of the degassed zircons was measured at the University of Melbourne (Additional file 1: Text S3).

Analytical results and geo-/thermo-chronologic interpretations

Fluid-inclusion analyses

It was difficult to find fluid inclusions suitable for measurement, mainly because of the low transparency of the majority of the fluid inclusions. Hence, the fluid inclusion analysis yielded only a relatively small number of measurements (Table 2). The homogenization temperatures were estimated to be 140–145 °C ($n = 3$) for HJG1-F and 110–216 °C ($n = 10$) for HJG2-F. By measuring only primary inclusions, reproducible results were obtained for each of these two samples, ranging between 144 and 145 °C for HJG1-F and 195–211 °C for HJG2-F. We interpreted these temperatures as reflecting fluid temperatures at the time of formation of the alteration zones. No data were obtained for HJG4-F owing to the lack of two-phase fluid inclusions. The wide range of homogenization temperatures obtained from the secondary inclusions in HJG2-F may indicate diverse fluid activity at different temperatures and probably at various periods after initial formation of the alteration zone. The final ice-melting temperatures were difficult to measure owing to the small size of the fluid inclusions. Only six measurements (including those from secondary inclusions) were obtained from HJG2-F, yielding final ice-melting temperatures of − 5.0 °C to − 0.4 °C and salt concentrations of 0.7 wt% to 7.9 wt%.

Zircon U–Pb analyses

Among the zircon U–Pb dating results for the sedimentary and alteration zone samples (Additional file 2: Figs. S1 and Additional file 3: Fig. S2; Additional file 10:

Table 2 Summary of fluid inclusion data

Inclusion No	Mineral	Inclusion type	T_h [°C]	T_{fim} [°C]	Salt conc. [wt% NaCl]	Note
HJG1-F						
1–1	Qtz	I	**145**	–	–	
1–2	Qtz	II	140	–	–	
1–3	Qtz	II	–	–	–	T_h and T_{fim} were not obtained
1–4	Qtz	II	–	–	–	T_h and T_{fim} were not obtained
1–5	Qtz	II	–	–	–	T_h and T_{fim} were not obtained
1–6	Qtz	II	–	–	–	T_h and T_{fim} were not obtained
1–7	Qtz	II	–	–	–	T_h and T_{fim} were not obtained
1–8	Qtz	II	–	–	–	T_h and T_{fim} were not obtained
1–9	Qtz	II	–	–	–	T_h and T_{fim} were not obtained
1–10	Qtz	I	**144**	–	–	
HJG2-F						
2–1	Qtz	II	186	-1.0	1.7	
2–2	Qtz	II	–	–	–	T_h = 62 °C but not reproducible
2–3	Qtz	II	–	–	–	T_h = 104 °C but not reproducible
2–4	Qtz	II	–	–	–	T_h = 132 °C but not reproducible
2–5	Qtz	II	117	–	–	
2–6	Qtz	II	214	–	–	
2–7	Qtz	II	173	–	–	
2–8	Qtz	II	173	-0.4	0.7	
2–9	Qtz	II	–	–	–	T_h = 118 °C but not reproducible
2–10	Qtz	II	–	–	–	T_h = 110 °C but not reproducible
2–11	Qtz	I	**195**	**-5.0**	**7.9**	
2–12	Qtz	I	**211**	-	-	
2–13	Qtz	II	187	-5.0	7.9	
2–14	Qtz	II	110	–	–	
2–15	Qtz	II	–	–	–	T_h = 110 °C but not reproducible
2–16	Qtz	II	–	− 4.5	7.2	
2–17	Qtz	II	216	− 2.9	4.8	
HJG4-F						
4–1	Qtz	II	–	–	–	Monophase liquid inclusion
4–2	Qtz	II	–	–	–	Gaseous inclusion
4–3	Qtz	II	–	–	–	Gaseous inclusion
4–4	Qtz	II	–	–	–	Gaseous inclusion
4–5	Qtz	II	–	–	–	Gaseous inclusion
4–6	Qtz	II	–	–	–	Gaseous inclusion
4–7	Qtz	II	–	–	–	Gaseous inclusion
4–8	Qtz	II	–	–	–	Monophase liquid inclusion
4–9	Qtz	II	–	–	–	Monophase liquid inclusion
4–10	Qtz	II	–	–	–	Monophase liquid inclusion
4–11	Qtz	II	–	–	–	Gaseous inclusion
4–12	Qtz	II	–	–	–	Gaseous inclusion
4–13	Qtz	II	–	–	–	Monophase liquid inclusion
4–14	Qtz	II	–	–	–	Monophase liquid inclusion
4–15	Qtz	II	–	–	–	Monophase liquid inclusion
4–16	Qtz	I	–	–	–	Monophase liquid inclusion

Inclusion classification based on Roedder's (1984) criteria. [conc., concentration; I, primary inclusion type; II, secondary inclusion type; Qtz, quartz; T_{fim}, final ice-melting temperature; T_h, homogenization temperature, in bold if for primary inclusion]

Table S3), the grain ages generally indicate a few populations (Additional file 2: Fig. S1). In this study, we estimated the maximum depositional age (MDA) of the samples from their grain ages. For each sample, we calculated the weighted mean ^{238}U–^{206}Pb age from concordant age grains belonging to the youngest grain cluster at 2σ (YC2σ; Dickinson and Gehrels 2009). For two samples, HJG2-F and HJG4-10 m, MDA was obtained from the youngest single-grain age (YSG; Dickinson and Gehrels 2009) because the youngest grain cluster at ± 2σ comprised less than three grains (Table 3). The computed MDAs (± 1σ) range from 74.7 ± 4.1 Ma to 59.2 ± 4.0 Ma (Table 3; Additional file 3: Fig. S2). For the sedimentary and alteration zone samples, the ablation spots were determined in agreement with the areas in which spontaneous tracks were counted for simultaneously obtaining FT dates. Therefore, these U–Pb dates may contain older dates obtained from the inherited cores (see Fig. 6 of Malusá and Fitzgerald 2020). However, it is not critical for estimation of the MDAs if enough numbers of grains are measured.

Among the U–Pb dating results for the Omine Acidic Rocks (Additional file 4: Fig. S3; Additional file 10: Table S3), sample HJG3-Upb produced eight discordant ages from 25 measurements (Additional file 4: Figs. S3a and b), which is probably related to the common Pb contamination from tiny inclusions. Therefore, we used the weighted mean obtained from the 17 concordant ^{238}U–^{206}Pb ages, 14.87 ± 0.57 Ma (± 2σ) (Additional file 4: Fig. S3c). As a secondary standard, OD-3 zircons were simultaneously measured with the unknown samples, yielding a concordia age of 32.6 ± 0.94 Ma (± 1σ) (Additional file 4: Fig. S3d) which is concordant with the reference age (33.0 ± 0.1 Ma (± 2σ); Iwano et al. 2013), thereby providing independent support for the accuracy of our results. For the intrusive rock samples, U–Pb dating was carried out on rims of the zircon grains with reference to the cathodoluminescence images. Therefore, the dates are expected to approximate the crystallization ages (see Fig. 6 of Malusá and Fitzgerald 2020).

Table 3 Summary of zircon U–Pb data for sedimentary rocks and alteration zones

Sample code	All grains	YC2σ		YSG
		n	Age ± 1σ [Ma]	Age ± 1σ [Ma]
HJG1-F	30	12	**73.9 ± 2.7**	68.6 ± 1.9
HJG1-0–5 cm	30	7	**70.0 ± 2.9**	65.5 ± 2.0
HJG1-5–10 cm	30	4	**65.9 ± 4.3**	59.6 ± 2.7
HJG1-0 m	28	6	**72.0 ± 5.1**	66.7 ± 2.1
HJG1-1 m	30	8	**71.1 ± 3.7**	64.3 ± 2.5
HJG1-3 m	30	10	**74.7 ± 4.1**	69.1 ± 2.6
HJG1-10 m	30	15	**71.9 ± 3.7**	65.9 ± 3.6
HJG1-20 m	30	4	**66.4 ± 6.5**	57.3 ± 3.2
HJG2-F	30	2	63.0 ± 4.2	**60.3 ± 1.8**
HJG2-0–5 cm	30	13	**74.2 ± 2.0**	70.4 ± 2.2
HJG2-5–10 cm	30	10	**74.6 ± 3.6**	69.0 ± 2.6
HJG2-0 m	30	5	**63.5 ± 4.4**	55.2 ± 3.8
HJG2-1 m	30	14	**73.2 ± 5.0**	67.0 ± 4.5
HJG2-3 m	30	7	**71.2 ± 4.8**	64.1 ± 2.7
HJG2-10 m	30	4	**63.7 ± 5.1**	57.8 ± 2.4
HJG4-0 m	30	4	**69.1 ± 5.3**	62.0 ± 2.8
HJG4-1 m	30	4	**69.5 ± 5.4**	61.7 ± 2.5
HJG4-3 m	30	5	**71.2 ± 3.0**	66.6 ± 2.6
HJG4-10 m	30	1	59.2 ± N/A	**59.2 ± 4.0**

YC2σ: youngest grain cluster at 2σ; YSG: youngest single grain (Dickinson and Gehrels 2009; Coutts et al. 2019). Bold font indicates the maximum depositional age adopted. YC2σ is expected to be calculated from three or more grains; therefore, the estimates for HJG2-F and HJG4-10 m were not adopted as the maximum depositional age (Additional file 3: Fig. S2)

Fission-track analyses

We obtained pooled FT ages (± 1σ) ranging from 48.7 ± 1.9 to 24.0 ± 1.1 Ma for zircons from the sedimentary and alteration-zone samples (Table 4). Based on radial plots (Galbraith 1990) and finite mixture model (Galbraith and Green 1990), the zircon grains were grouped into up to three age populations for each sample. Cluster 1 is the youngest population of < ~ 31 Ma, cluster 2 is the population of ~ 54–38 Ma equivalent to the approximate depositional age in the Eocene (Suzuki 1993; Tokiwa et al. 2016), and cluster 3 is the population of > ~ 76 Ma, which is older than the depositional age (Table 5, Additional file 5: Fig. S4). The FT length data for zircon showed a bimodal distribution for all sedimentary and alteration zone samples, consisting of shorter tracks of < ~ 8 μm and longer tracks of ~ 11 μm (Additional file 6: Fig. S5). The ages of the youngest population did not show a clear trend with respect to distance from the alteration zones, and were dispersed over the range of uncertainties between the samples (Fig. 7). This overdispersion might be derived from a combination of the partial resetting of FT ages, as evidenced by the bimodal FT length (Additional file 6: Fig. S5), and the variation in the crystallization ages of the youngest zircons, as shown by the scattered youngest zircon U–Pb ages (Fig. 7).

Apatite for the sedimentary and alteration-zone samples produced pooled FT ages (± 1σ) ranging from 14.9 ± 2.1 to 9.0 ± 1.0 Ma (Table 4). The pooled ages were homogeneous, and did not show an obvious tendency with respect to their locations relative to the alteration zones (Fig. 7). Given the low FT densities (Table 4), only a few FT lengths (n = 1–13) were measured on apatite for each sample, although some samples included tracks shorter than the assumed initial length (~ 14–15 μm) (Additional file 7: Fig. S6). ^{252}Cf-irradiation

Table 4 Summary of AFT and ZFT data

Sample code	Grains	Spontaneous FT		U measurement		U standard		U [ppm]	ζ value [cm^2/year]	Pooled FT age ± 1σ [Ma]	Cl [wt%]
		ρ_s [10^6 cm^{-2}]	N_s	ρ_U [10^9 cm^{-2}]	N_U	$\rho_{U\text{-}std}$ [10^9 cm^{-2}]	$N_{U\text{-}std}$				
Zircon											
HJG1-F	30	4.37	970	18.30	4230785	5.279	47513	291	42.5 ± 1.2	25.7 ± 1.2	–
HJG1-0–5cm	30	7.36	1986	16.90	4554139	5.279	47513	268	42.5 ± 1.2	48.7 ± 1.9	–
HJG1-5–10cm	30	6.43	1735	22.10	5954473	4.971	44741	373	42.5 ± 1.2	30.7 ± 1.2	–
HJG1-0m	28	4.77	1164	5.59	1367571	1.333	15697	352	46.8 ± 1.0	26.5 ± 1.2	–
HJG1-1m	30	6.47	1657	6.35	1619317	1.430	16835	373	46.8 ± 1.0	34.1 ± 1.4	–
HJG1-3m	30	5.51	1389	6.08	1511646	1.359	16006	376	46.8 ± 1.0	29.2 ± 1.3	–
HJG1-10m	30	5.10	1335	6.15	1596112	1.345	15835	384	46.8 ± 1.0	26.3 ± 1.1	–
HJG1-20m	30	4.15	1192	5.13	1461429	1.356	15972	318	46.8 ± 1.0	25.8 ± 1.2	–
HJG2-F	30	7.69	2076	21.40	5766492	4.971	44741	361	42.5 ± 1.2	37.9 ± 1.5	–
HJG2-0–5cm	30	6.75	1822	20.10	5431976	4.783	43043	353	42.5 ± 1.2	34.0 ± 1.3	–
HJG2-5–10cm	30	8.97	2422	20.90	5655631	4.783	43043	368	42.5 ± 1.2	43.4 ± 1.6	–
HJG2-0m	30	4.23	1121	5.55	1440745	1.345	15842	347	46.8 ± 1.0	24.5 ± 1.1	–
HJG2-1m	30	4.20	1108	4.55	1188763	1.341	15791	285	46.8 ± 1.0	29.2 ± 1.4	–
HJG2-3m	30	3.90	1111	5.02	1367704	1.349	15883	313	46.8 ± 1.0	25.6 ± 1.2	–
HJG2-10m	30	4.52	1312	4.62	1301212	1.320	15540	294	46.8 ± 1.0	31.1 ± 1.4	–
HJG3-Upb	36	3.10	1733	23.30	12849644	5.022	45194	390	48.6 ± 2.2	16.4 ± 0.8	–
HJG4-0m	30	3.78	993	5.05	1323100	1.369	16116	310	46.8 ± 1.0	24.0 ± 1.1	–
HJG4-1m	30	4.67	1229	4.97	1307709	1.299	15299	322	46.8 ± 1.0	28.5 ± 1.3	–
HJG4-3m	30	5.60	1293	6.33	1405870	1.238	14581	429	46.8 ± 1.0	26.6 ± 1.2	–
HJG4-10m	30	5.41	1559	6.14	1743630	1.186	13967	435	46.8 ± 1.0	24.8 ± 1.0	–
Apatite											
HJG1-0–5cm	29	0.228	82	3.94	1416827	1.616	14541	34	253 ± 18	11.8 ± 1.6	0.22
HJG1-5–10cm	28	0.194	70	2.49	897322	1.511	13599	23	253 ± 18	14.9 ± 2.1	0.15
HJG1-0m	36	0.182	103	0.65	370749	0.3119	3820	29	254 ± 18	11.0 ± 1.5	0.16
HJG1-1m	36	0.201	164	0.90	718624	0.3119	3820	40	254 ± 18	9.0 ± 1.0	0.24
HJG1-3m	36	0.187	161	0.74	640728	0.3119	3820	33	254 ± 18	9.9 ± 1.1	0.15
HJG1-10m	30	0.174	129	0.66	481343	0.3225	3951	29	254 ± 18	11.0 ± 1.3	0.14
HJG1-20m	30	0.274	194	0.12	824188	0.3225	3951	52	254 ± 18	9.6 ± 1.0	0.29
HJG2-F2	30	0.244	88	2.32	834729	0.9654	8688	34	253 ± 18	12.9 ± 1.7	0.11
HJG2-0–5cm	30	0.253	91	2.03	732329	0.6609	5948	43	253 ± 18	10.4 ± 1.4	0.21
HJG2-5–10cm	30	0.208	75	0.65	234188	0.3685	3317	25	253 ± 18	14.9 ± 2.2	0.57
HJG2-0m	30	0.359	255	0.12	868650	0.3225	3951	51	254 ± 18	12.0 ± 1.2	0.31
HJG2-1m	30	0.246	170	0.94	639748	0.3169	3883	41	254 ± 18	10.7 ± 1.2	0.36

Table 4 (continued)

Sample code	Grains	Spontaneous FT		U measurement		U standard		U [ppm]	ζ value [cm^2/year]	Pooled FT age ± 1σ [Ma]	Cl [wt%]
		ρ_s [10^6 cm^{-2}]	N_s	ρ_U [10^9 cm^{-2}]	N_U	$\rho_{U\text{-std}}$ [10^9 cm^{-2}]	$N_{U\text{-std}}$				
HJG2-3m	30	0.203	132	0.70	430783	0.3169	3883	31	254 ± 18	12.3 ± 1.5	0.64
HJG2-10m	30	0.187	125	0.82	517618	0.3169	3883	36	254 ± 18	9.7 ± 1.2	0.33
HJG3-Upb	30	0.0187	14	0.23	174686	1.674	20512	2	262 ± 24	17.5 ± 5.1	0.004
HJG4-0m	18	0.272	68	0.10	283953	0.3104	3803	46	254 ± 18	9.4 ± 1.4	0.14
HJG4-1m	30	0.123	82	0.44	272067	0.3104	3803	20	254 ± 18	11.9 ± 1.7	0.14
HJG4-3m	30	0.202	134	0.79	514705	0.3104	3803	36	254 ± 18	10.2 ± 1.2	0.71
HJG4-10m	30	0.242	177	0.88	605794	0.3104	3803	40	254 ± 18	11.5 ± 1.3	0.23

The apatite chlorine content is correlated with the AFT annealing rate (e.g., Carlson et al. 1999). The pooled fission-track ages (t) and their errors (σ) were calculated using the following equations:

$$t = \frac{1}{\lambda_D} ln\left(1 + \lambda_D \bullet g \bullet \zeta \frac{\sum N_s}{\sum N_U} \rho_{U-std}\right)$$

$$\sigma = t\sqrt{\frac{1}{\sum N_s} + \frac{1}{\sum N_U} + \frac{1}{\sum N_{U-std}} + \left(\frac{\sigma_\zeta}{\zeta}\right)^2}$$

where λ_D is total decay constant of ^{238}U (= 1.55125×10^{-10} year^{-1}), and g is geometry factor (= 0.5 for internal surfaces). Nancy 91500 zircon and Durango apatite were used as uranium standards (Additional file 1: Text S2). [Cl, chlorine content; N_s, number of spontaneous tracks; N_U, number of uranium measurements on unknowns; $N_{U\text{-std}}$, number of uranium measurements on standard; ρ_s, density of spontaneous tracks; ρ_U, density of uranium measurements on unknowns; $\rho_{U\text{-std}}$, density of uranium measurements on standard; U, uranium content; ζ, zeta calibration factor; σ_ζ, error of zeta calibration factor]

Table 5 Summary of age clusters of ZFT data

Sample code	n	Central age ± 1σ [Ma]	MSWD	P(χ^2)	Dispersion ± 95%CI [%]			Cluster 1 ± 1σ [Ma]	Cluster 2 ± 1σ [Ma]	Cluster 3 ± 1σ [Ma]
HJG1-F	30	24.54 ± 3.89	26	0	83.50	+ 29.6	− 20	22.96 ± 0.93		127.30 ± 8.68
HJG1-0-5 cm	30	37.06 ± 4.61	28	0	65.8	+ 22.0	− 15	22.86 ± 1.30	53.98 ± 2.57	113.03 ± 4.07
HJG1-5-10 cm	30	27.55 ± 2.66	17	0	50.2	+ 17.3	− 12	16.59 ± 1.04	38.34 ± 1.19	122.4 ± 10.8
HJG1-0 m	28	26.53 ± 1.92	6.2	0	34.40	+ 13.65	− 9.3	23.48 ± 0.91	44.99 ± 2.87	
HJG1-1 m	30	33.71 ± 2.36	9.9	0	34.99	+ 12.63	− 8.5	26.70 ± 1.37	39.48 ± 2.22	90.36 ± 6.19
HJG1-3 m	30	28.21 ± 1.76	5.5	0	29.98	+ 11.68	− 8.1	25.40 ± 0.86	48.01 ± 2.48	
HJG1-10 m	30	26.85 ± 2.30	11	0	43.8	+ 15.3	− 10	26.35 ± 0.75		166.0 ± 21.3
HJG1-20 m	30	25.28 ± 2.07	8.4	0	40.6	+ 14.9	− 10	20.83 ± 1.55	43.62 ± 3.86	
HJG2-F	30	33.42 ± 2.90	15	0	44.2	+ 15.8	− 11	27.18 ± 1.05	45.62 ± 1.79	96.47 ± 5.36
HJG2-0-5 cm	30	29.84 ± 3.91	31	0	69.6	+ 23.2	− 15	26.82 ± 0.80		103.28 ± 4.31
HJG2-5-10 cm	30	38.16 ± 4.29	28	0	59.6	+ 19.9	− 13	30.88 ± 0.99		91.15 ± 3.14
HJG2-0 m	30	24.13 ± 1.84	6.7	0	37.55	+ 14.20	− 9.7	26.63 ± 0.80		
HJG2-1 m	30	28.63 ± 2.19	6.9	0	37.65	+ 14.19	− 9.7	24.61 ± 1.13	49.29 ± 3.08	
HJG2-3 m	30	25.38 ± 1.26	2.6	3.4E-06	20.72	+ 10.29	− 7.8	26.49 ± 0.80		
HJG2-10 m	30	29.49 ± 2.75	12	0	47.7	+ 16.8	− 11	21.27 ± 1.00	46.24 ± 1.96	116.6 ± 12.4
HJG4-0 m	30	24.18 ± 1.31	2.9	2.1E-07	22.98	+ 10.93	− 8.1	25.03 ± 0.80		
HJG4-1 m	30	28.27 ± 2.17	8.4	0	38.15	+ 14.26	− 9.6	26.04 ± 0.82		76.34 ± 5.52
HJG4-3 m	30	26.42 ± 1.55	4.3	8.2E-14	27.33	+ 11.50	− 8.1	23.61 ± 0.92	41.42 ± 2.68	
HJG4-10 m	30	24.28 ± 1.85	9.3	0	38.37	+ 13.77	− 9.3	23.15 ± 0.65		59.75 ± 3.94

The parameters were calculated using IsoplotR (Vermeesch 2018). [MSWD, mean square weighted deviation; P(χ^2), the p-value of a chi-square probability for homogeneity; 95%CI, 95% confidence interval]

was performed on apatite in an effort to increase the confined tracks (Donelick and Miller 1991), but large etch pits obscured the identification and measurement of the confined tracks. The chlorine content of the apatite was also measured as a kinetic parameter (e.g., Carlson et al. 1999). The mean values range from 0.11 to 0.71 wt% for the sedimentary and alteration-zone samples (Table 4).

Quartz porphyry sample (HJG3-Upb) yielded pooled FT ages (± 1σ) of 16.4 ± 0.8 Ma on zircon and 17.5 ± 5.1 Ma on apatite (Table 4). These ages are in broad agreement with the zircon U–Pb age of 14.87 ± 0.57 Ma (± 2σ) within the error range. The ZFT length exhibited a monomodal distribution with a mean length comparable to the initial length (~ 11 μm) (Additional file 6: Fig. S5). This sample is interpreted as having cooled below the closure temperature of the ZFT system (~ 300 °C) immediately after intrusion.

(U–Th)/He analyses

We performed ZHe dating of grains from HJG1 and HJG2 samples and simultaneously analyzed Fish Canyon Tuff reference zircons as an additional check on analytical accuracy (Table 6). The weighted mean age of 27.7 ± 3.1 Ma for Fish Canyon tuff is consistent with the reference value, 28.3 ± 0.4 Ma (Gleadow et al. 2015), implying accuracy of dating results for our unknowns. The relative error of the weighted mean age of Fish Canyon Tuff zircons (1σ = ~ 11.2%) was adopted as the total uncertainty of our (U-Th)/He analytical procedures and was applied to the error of the single-grain ages of the unknowns (Table 6). Single-grain ages of the unknowns are in the range ~ 23.6–8.7 Ma, except for two outliers (HJG2-10 m-006 and HJG1-20 m-010). HJG2-10 m-006 may be monazite, considering its extremely high U and Th content. HJG1-20 m-010 might have been incompletely digested because it had the lowest Th content. Taking into account the different ranges of closure temperatures, the weighted mean age of the other grains, 16.8 ± 3.9 Ma, is consistent with the ZFT and AFT ages. Although this ZHe age is also consistent with the zircon U–Pb, ZFT, and AFT ages of HJG3-Upb, it is discussed in Sect. 6.1, along with their geological implications.

As with the other thermochronometers, the ZHe dates did not show a clear trend with distance from the alteration zones. However, the single-grain ages were dispersed beyond the range of uncertainties for a few samples (e.g., HJG1-1 m, HJG1-10 m, and HJG2-0 m), which can be attributed to various factors. For example, we cannot deny the possible effects of He-rich inclusions or the heterogeneous distribution of parent isotopes (e.g., Danišík et al. 2017). Alternatively, differences in the amount of radiation damage and subsequent differences in the closure temperature (Guenthner et al. 2013) are also plausible, considering that the samples contain zircons with

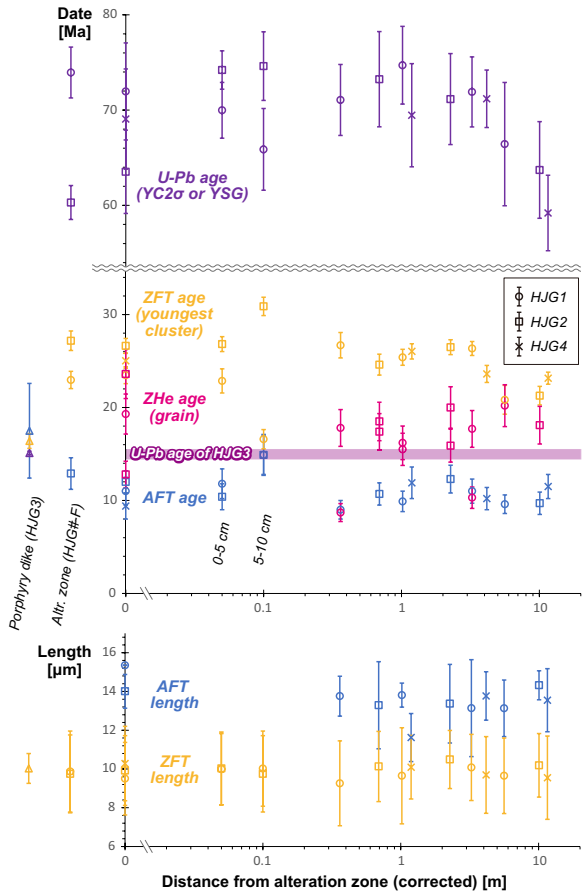

Fig. 7 Thermochronometric data plotted against distance from alteration zones. The distances were calibrated against the strike and dip of the alteration zones. Error bars for data are ± 1 standard error for FT lengths and ± 1σ for FT ages and U–Pb ages. The ZHe data were plotted as single-grain ages ± 1σ

various crystallization ages (Additional file 2: Fig. S1). However, it is difficult to specify the main factor because of the small number of grains measured. Hence, the ZHe dates are regarded as reference data.

Geological implications

Thermal effects by the quartz porphyry dike intrusion

Before discussing possible thermal anomalies related to hydrothermal activity, we need to evaluate the thermal effects of the quartz porphyry dike intrusion. The horizontal distance from the sample locations to the dike margins is ~ 200 m for HJG1, and ~ 100 m for HJG2 and HJG4, whereas the dike width is ~ 100 m (Fig. 5). Considering the subvertical (82°N) dip of the boundary between the dike and host rocks, these distances approximate the true three-dimensional distances. Matsuzaki et al. (2004) simulated the thermal effects of a 50-m-thick pyroclastic flow on the host rocks, showing the annealing of FTs of the host rock within ~ 20 m for zircon and within ~ 100 m for apatite from the boundary. Therefore, under the conditions of this study, apatite FTs might have been annealed by the dike intrusion, depending on thermal conditions, such as, ambient temperature, thermal conductivity of the rocks, and duration over which the magma remained hot. However, this is less possible for the following reasons: (1) AFT ages from the three locations are younger than the intrusion age of ~ 15 Ma obtained from HJG3; (2) AFT ages from the three locations are comparable regardless of the difference in distance from the dike margin; and (3) some AFTs are shorter than the initial length (~ 14–15 μm), which is inconsistent with a total annealing scenario due to reheating (Additional file 7: Fig. S6).

Thermal anomalies by the hydrothermal activities

From the spatial patterns of the thermochronometric data plotted against the distance from the alteration zones (Fig. 7), we observed no significant variation in any system or parameter, even in the AFT system, which had the lowest closure temperature among the systems explored. Compared with the model predictions (Fig. 4), the observations can be explained by the two scenarios below. First, the cooling dates reflect regional cooling and exhumation rather than local reheating by fluid activity, as shown in the case of $T_f = 150$ °C (or lower T_f). Alternatively, the cooling dates may reflect reheating by fluid activity, as shown in the case of $T_f = 200$ °C, showing spatially uniform resetting within a few meters of the alteration zones. In the latter case, the AFT and ZHe systems are expected to have been totally and partially reset, respectively, depending on the heating duration although the ZFT system is not expected to have been reset significantly. Nonetheless, this case is less likely because AFTs shorter than the initial length were observed in some samples (Additional file 7: Fig. S6). Consequently, the cooling dates obtained are considered to have been derived from regional thermal and exhumation histories. Based on a comparison with the model predictions (Fig. 4), it is concluded that fluid activity did not affect the cooling dates, probably because the heating duration was too short (e.g., less than ~ 10 years at HJG2 with $T_f = \sim 200$ °C) and/or fluid activity occurred at a greater depth before the regional thermal/exhumation events and was later overprinted by regional events (see also Fig. 8.7 of Malusá and Fitzgerald (2019b) for more comprehensive concepts about impacts of exhumation vs reheating on cooling dates).

Regional thermal and exhumation history of accretionary complexes

The regional thermal and exhumation histories of accretionary complexes in the study area are constrained using

Table 6 Summary of zircon (U–Th)/He data

Sample code	Grain ID	Mass [μm]	^{238}U [ppm]	^{232}Th [ppm]	Th/U	^{4}He [ncc/mg]	F_T	eU [ppm]	(U-Th)/He age ± 1σ [Ma]	
									Raw	Corr
Unknown									Weighted mean age ± 1σ:	**16.8** ± 3.9
HJG1-0 m	008	2.8	–	–	–	1665.3	–	–	–	–*
	015	1.3	302.0	162.7	0.54	477.4	0.60	340.3	11.5	19.3 ± 2.2
HJG1-1 m	010	2.8	481.2	242.7	0.50	827.8	0.71	538.2	12.6	17.8 ± 2.0
	003	2.4	584.4	294.2	0.50	489.0	0.71	653.5	6.2	8.7 ± 1.0
HJG1-3 m	008	2.2	256.8	129.0	0.50	374.1	0.69	287.1	10.7	15.5 ± 1.7
	004	3.7	570.2	212.8	0.37	910.8	0.75	620.2	12.1	16.2 ± 1.8
HJG1-10 m	009	3.1	901.1	292.4	0.32	1539.6	0.74	969.8	13.0	17.7 ± 2.0
	013	4.0	605.4	147.6	0.24	585.9	0.73	640.1	7.5	10.3 ± 1.2
HJG1-20 m	006	4.9	312.7	181.5	0.58	652.0	0.75	355.4	15.1	20.2 ± 2.3
	010	6.2	163.7	68.9	0.42	901.2	0.77	179.8	41.1	53.4 ± 6.0**
HJG2-0 m	002	4.6	147.2	128.0	0.87	210.9	0.76	177.3	9.8	12.8 ± 1.4
	004	5.7	171.6	110.2	0.64	438.1	0.77	197.5	18.2	23.6 ± 2.6
HJG2-1 m	006	1.9	573.4	372.7	0.65	956.0	0.68	660.9	11.9	17.4 ± 1.9
	009	1.7	483.1	481.1	1.00	864.2	0.64	596.2	11.9	18.5 ± 2.1
HJG2-3 m	003	5.3	659.8	179.8	0.27	1295.3	0.76	702.0	15.2	20.0 ± 2.2
	010	2.2	274.5	133.2	0.49	415.8	0.70	305.8	11.2	15.9 ± 1.8
HJG2-10 m	006	3.7	5122.1	12,243.4	2.39	635.9	0.73	7999.3	0.7	0.9 ± 0.1**
	009	3.8	309.1	176.4	0.57	554.9	0.72	350.5	13.0	18.1 ± 2.0
Fish Canyon Tuff: 28.3 ± 0.4 Ma (ZHe age ± 1σ; Gleadow et al. 2015)									Weighted mean age ± 1σ:	27.7 ± 3.1
FCT3	013	5.1	217.9	93.5	0.43	978.0	0.76	239.9	19.7	24.5
	103	9.8	356.9	213.0	0.60	1106.5	0.80	406.9	22.3	27.8
	108	4.5	342.0	182.1	0.53	1066.0	0.74	384.8	22.7	30.7

[a] F_T is the α-ejection correlation (Farley et al. 1996; Hourigan et al. 2005). Proxy for alpha-radiation activity is computed as eU = [U] + 0.235[Th] (Shuster et al. 2006).
[*sample lost during U–Th measurement; **not included in weighted mean calculations; Corr., corrected; eU, effective uranium concentration]

the thermochronological data. Data from 19 samples (17 sedimentary and 2 alteration zone samples) were integrated (Fig. 8) because they were collected within a range of < ~ 1 km (Fig. 5) and therefore would be expected to share a common thermal history with no local thermal disturbances. The integration resulted in pooled FT ages (± 1σ) of 10.9 ± 0.8 Ma (n = 545) for apatite and mean FT length of 13.51 ± 1.60 μm (n = 67) for apatite and 9.82 ± 1.91 μm (n = 625) for zircon. For zircon, a central age of 28.3 ± 0.6 Ma (n = 568) was calculated rather than the pooled FT ages because the single-grain dates were grouped into four clusters. Although the number of FT length data for each sample is small for apatite, the integration shows a negatively skewed unimodal distribution, which is consistent with that of slowly cooled bedrock (e.g., Gleadow et al. 1986). Using the integrated FT age and length data, we applied thermal inversion modeling using HeFTy v.1.9.3 software (Ketcham 2005) (Additional file 1: Text S4). Thermal inversion was performed assuming a history of burial and exhumation (Fig. 8d). The AFT and ZFT data were incorporated into the inversion based on the annealing kinetics of Ketcham et al. (2007) and fanning linear model of Yamada et al. (2007). As HeFTy utilizes pooled FT ages for the inversion, the pooled FT ages for zircon were recalculated to be 21.4 ± 0.5 Ma (± 1σ) from 373 grains belonging to the peak 2, and this was adopted for the inversion. ZHe data were not used for the inversion because it was difficult to address the causes of the over-dispersed grain ages owing to the small number of measurements, as noted in Sect. "(U–Th)/He analyses".

In this study, we found that the ZFT lengths have a bimodal distribution, generally implying a reheating episode or long residence time within the ZFT PAZ (with subsequent cooling below the ZFT PAZ), and ZFT grain ages that are generally younger than the Eocene depositional age (Fig. 8b and c). Considering that ZFT ages of ~ 80–70 Ma have been reported for the Southern Shimanto Belt in adjacent areas (Umeda et al. 2007; Hanamuro et al. 2008), the younger ZFT ages in this study may have been partially reset by a reheating episode related to heat influx in the Miocene (Hasebe and Watanabe 2004).

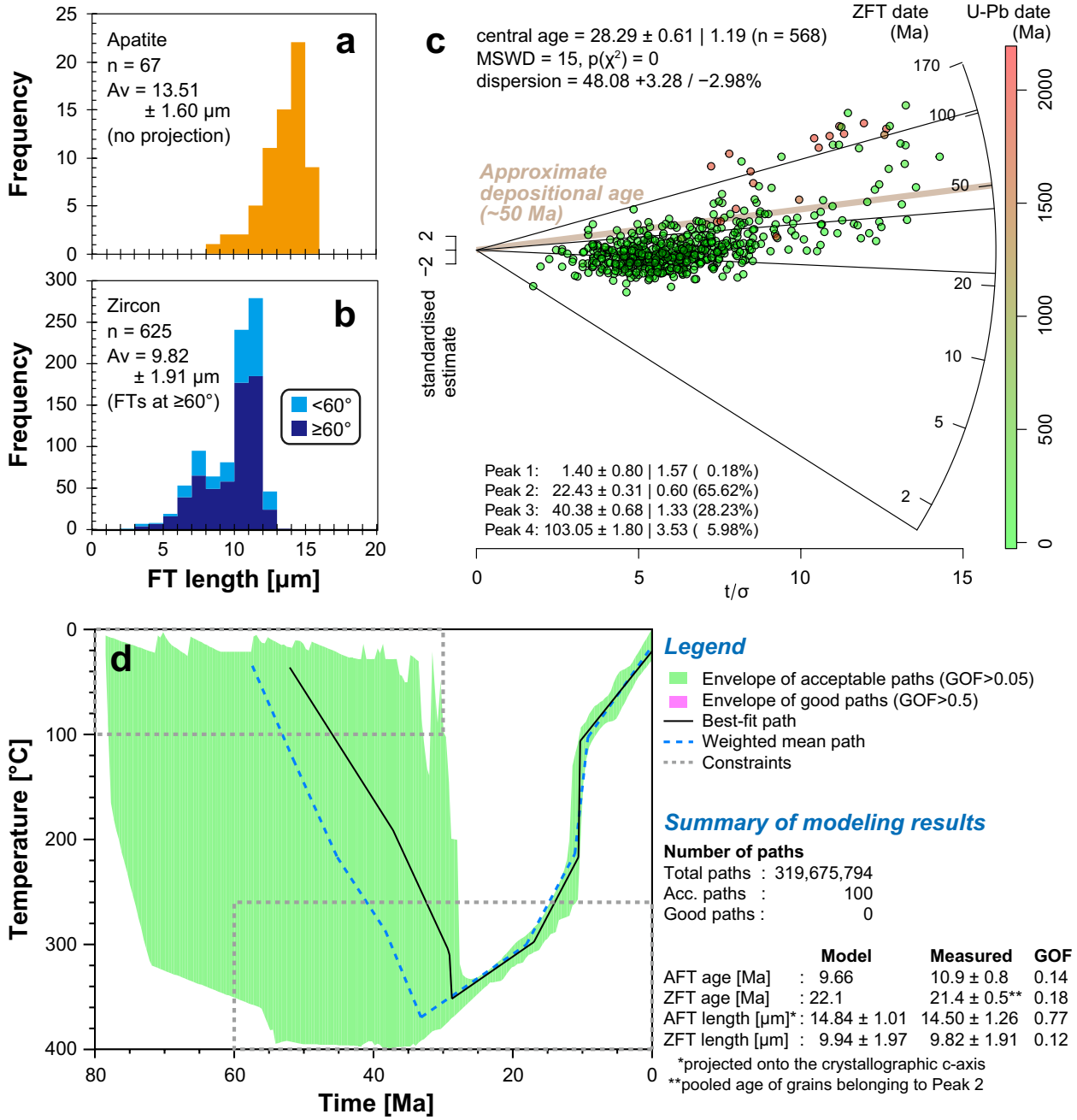

Fig. 8 Fission-track length histograms of (**a**) apatite and (**b**) zircon, integrated for 17 sedimentary and two alteration zone samples studied (Additional file 6: Figs. S5 and Additional file 7: Fig. S6). The track length distribution of zircon is shown with different infill colors for tracks marking azimuth angles that are higher (dark blue column) and lower (light blue column) than 60° to the crystallographic *c*-axis, because track lengths in zircon are dependent on etching and annealing properties, which exhibit angular variation (Hasebe et al. 1994; Yamada et al. 1995). **c** Radial plots (Galbraith 1990) of ZFT ages integrated for 19 samples. Plots were drawn using IsoplotR software (Vermeesch 2018). **d** Inverse-thermal-history models based on integrated FT ages and FT length data. Modeling was carried out using HeFTy v.1.9.3 software (Ketcham 2005). The constraints were determined based on geological and geochronological evidence to reconstruct burial and exhumation of the Haroku Formation (Additional file 1: Text S4). No good paths were obtained from the generated paths. [Acc., acceptable; Av, mean length ± 1σ; GOF, goodness of fit; *n*, population size; N, number of fission-track lengths measured]

Considering that the study area is in the northern part of the Southern Shimanto Belt and lies between two locations where AFT ages of ~ 13 Ma and ~ 6 Ma have been reported (Hasebe and Tagami 2001), the AFT ages of ~ 10 Ma reported here are consistent with a southward younging trend. The AFT lengths exhibited a unimodal, negatively skewed distribution (Fig. 8a), which is typical of undisturbed bedrock (cf. Gleadow et al. 1986), indicating relatively slow cooling through the AFT PAZ. Although thermal inversion results prior to ~ 30 Ma are not well constrained by the thermochronometric data alone and depend strongly on other geological constraints, results indicate residence in the ZFT PAZ prior to ~ 15 Ma, subsequent rapid cooling between ~ 15 and 10 Ma through to the AFT PAZ, and slightly slower cooling from ~ 10 Ma to the present surface temperature (Fig. 8d).

Reheating to the ZFT PAZ until ~ 15 Ma might be related to the heat flux generated by the subsurface batholith of the middle Miocene acidic rocks (Hasebe and Watanabe 2004; Hoshi et al. 2022) rather than by burial of the accretionary complexes. Paleotemperatures of the Otonashigawa Group are estimated to be ~ 227 °C and ~ 192 °C (± > 50 °C) from illite crystallinity values (Awan and Kimura 1996), which are lower than the maximum temperature of the estimated thermal history (Fig. 8d). In fact, the ZFT dates of the Shimanto Belt without secondary heating events are generally older than ~ 50 Ma (Hasebe and Tagami 2001; Hasebe and Watanabe 2004; Ohira et al. 2016) (Fig. 2), which is older than the ZFT dates in this study. Several geophysical observations have suggested the presence of a subsurface pluton beneath the Kii Peninsula (e.g., Fuji-ta et al. 1997; Kodaira et al. 2006; Arnulf et al. 2022; Nakajima 2023). In addition, recent numerical studies have predicted that a subsurface pluton can affect the cooling ages at the surface, even if the pluton is not exposed at the surface (Murray et al. 2018). Based on these discussions, reheating to the ZFT PAZ until ~ 15 Ma is attributable to the heat flux of the subsurface batholith.

The cooling history from ~ 15 to 10 Ma is interpreted as reflecting regional cooling and exhumation of the accretionary complexes, likely associated with mountain development of the Outer Zone of the Southwest Japan Arc, that is, the Kii, Shikoku, and Kyushu mountains. Together with the AFT ages previously determined for the Kii Peninsula (Hasebe and Tagami 2001), Shikoku (Hasebe et al. 1993b, 1997) and Kyushu (Hasebe and Tagami 2001), these mountains are thought to have been exhumed through the AFT PAZ at ~ 10 Ma although only the Kii Mountains tilted northward. These mountains were uplifted mainly in the middle Miocene, and their exhumation slowed; by contrast, most other mountains on the islands of Japan were mainly uplifted under east–west compression since the late Pliocene (e.g., Yonekura et al. 2001). Mountains in the Outer Zone might have been exhumed by very different mechanisms, such as by the obduction of the SW Japan lithospheric sliver onto the Shikoku Basin (e.g., Yamaji and Yoshida 1998) or by rapid subduction (> 10 cm/year) of the Philippine Sea plate during the clockwise rotation of the Southwest Japan Arc at the end of the opening of the Sea of Japan (Kimura et al. 2005). However, obduction occurred at ~ 15 Ma (Yamaji and Yoshida 1998) and the clockwise rotation occurred at ~ 18–16 Ma (Hoshi et al. 2015; Hoshi 2018), showing a slight time-lag with the estimated rapid cooling at ~ 15–10 Ma (Fig. 8c). This time-lag might reflect a hiatus from the initiation of the uplift to the exhumation of the fossil AFT PAZ. Such a time-lag is more plausible in young mountains where the rock uplift rates and the exhumation rates are not in steady-state (e.g., Ahnert 1970; Ohmori 1978; Sueoka et al. 2016). Since the beginning of the uplift, a few million years are required to result in ~ 2–3 km of exhumation when uplifted at the rate of 0.1–1 mm/year (Fig. 5 of Sueoka et al. 2016).

Conclusions

We applied fluid-inclusion analyses and thermochronometry in an attempt to detect thermal anomalies around hydrothermal alteration zones in the Hongu area of the Southwest Japan Arc. The temperatures of the fluids at the time of formation of the alteration zones were estimated to be ~ 150 °C and ~ 200 °C based on the homogenization temperatures of the fluid inclusions. However, ZFT dates of ~ 27.2–16.6 Ma (the youngest cluster), ZHe dates of ~ 23.6–8.7 Ma (single-grain age) and AFT dates of ~ 14.9–9.0 Ma (pooled age) in host rocks show no consistent spatial variation with distance from the alteration zones. Considering the spatial variation and comparison with the model predictions, these cooling dates are interpreted as reflecting regional thermal and exhumation episodes rather than the thermal effects of hydrothermal fluid activity. Namely, fluid activity did not totally or partially reset adjacent host thermochronometers, probably because the duration of their activity was far too short or because the activity predated regional thermal/exhumation episodes. AFT ages of ~ 10 Ma may reflect mountain uplift and exhumation in the Outer Zone of the Southwest Japan Arc, which was possibly triggered by the obduction of the SW Japan lithospheric sliver onto the Shikoku Basin at ~ 15 Ma or by rapid slab subduction during clockwise rotation of the Southwest Japan Arc at ~ 18–16 Ma.

Abbreviations

FT	Fission track
AFT	Apatite fission track
ZFT	Zircon fission track
ZHe	Zircon (U–Th)/He
MDA	Maximum depositional age
YC2σ	Youngest grain cluster at 2σ
YSG	Youngest single grain age
eU	Effective uranium concentration
PAZ	Partial annealing zone
PRZ	Partial retention zone

Supplementary Information

The online version contains supplementary material available at https://doi.org/10.1186/s40623-023-01921-5.

Additional file 1. Text S1. Fluid-inclusion analyses. **Text S2.** FT and U–Pb analyses. **Text S3.** Zircon (U–Th)/He analyses. **Text S4.** Thermal-inverse calculations.

Additional file 2. Figure S1. Concordia plots of zircon U–Pb grain ages measured by Kyoto Fission-Track Co., Ltd. Error eclipses indicate a ±2σ range. The criteria for determining concordant/discordant ages and youngest-age populations are illustrated in **Supplementary Figure S2**. Plots were drawn using the Isoplot v.4.15 software (Ludwig, 2008).

Additional file 3. Figure S2. Zircon fission-track and U–Pb ages of single grains. The grains were arranged in descending order of the ^{238}U–^{206}Pb ages. The ^{238}U–^{206}Pb and ^{235}U–^{207}Pb ages were regarded as concordant when they overlapped within the range of ±2σ.

Additional file 4. Figure S3. Statistical plots of zircon U–Pb data measured at Tono Geoscience Center. (a, b) Concordia plots of quartz porphyry sample. (c) Weighted-mean ^{238}U–^{206}Pb ages of quartz porphyry sample. (d) Concordia plots of age standard OD-3 zircon (Iwano et al., 2012, 2013b). Plots were drawn using the Isoplot v.4.15 software (Ludwig, 2008). [MSWD, mean square weighted deviation].

Additional file 5. Figure S4. Radial plots of zircon FT single-grain ages. Plots were drawn using the IsoplotR software (Vermeesch, 2018). The age population peaks were determined using the finite mixture model (Galbraith and Green, 1990). p(χ2) is the probability of obtaining the χ2 value for ν degrees of freedom, where ν = (number of crystals − 1) (Galbraith, 1981). [MSWD, mean square weighted deviation; n, number of grains].

Additional file 6. Figure S5. Zircon FT length histograms. The track length distribution is shown using different fill colors for tracks indicating azimuth angles that are higher (dark blue column) and lower (light blue column) than 60° to the crystallographic c-axis, because track lengths in zircon depend on etching and annealing properties that show angular variation (Hasebe et al., 1994; Yamada et al., 1995). [Av, mean lengths ±1σ; N, number of track lengths measured].

Additional file 7. Figure S6. Apatite FT length histograms. The lengths were not projected onto the crystallographic c-axis. [Av, mean lengths ±1σ; N, number of track lengths measured].

Additional file 8. Table S1. Operating parameters for laser ablation inductively coupled plasma mass spectrometer at University of Tokyo. *1, Wiedenbeck et al. (1995); *2, Iwano et al. (2012); *3, Iwano et al. (2013b); *4, Lukács et al. (2015); *5, Sláma et al. (2008); *6, Jackson et al. (2004); *7, Danhara and Iwano (2013); *8, Iwano et al. (2018).

Additional file 9. Table S2. Operating parameters for laser ablation inductively coupled plasma mass spectrometer at Tono Geoscience Center. *1, Wiedenbeck et al. (1995); *2, Iwano et al. (2012); *3, Iwano et al. (2013b); *4, Lukács et al. (2015).

Additional file 10. Table S3. U-Pb isotopic date for zircon crystals determined by LA-ICP-MS.

Acknowledgements

Fluid inclusion analyses were performed by Geothermal Engineering Co., Ltd. We thank Kiyotaka Yoshikawa (JAEA) for supporting the sample preparation. Field trip and sample collection were supported by Tsuneari Ishimaru, Akiomi Shimada, Koji Shimada, Tetsuya Komatsu, Hiroki Amamiya, Tadamasa Ueki, Terumasa Tozawa, Hiroki Ogawa, Akira Goto, Shoma Fukuda (JAEA) and Messrs. Ura and Tani (Hongu branch office of Tanabe city office). Some figures were drawn using the Generic Mapping Tools (GMT; Wessel and Smith, 1991), 50-m mesh DEM and GSI Map of the Geospatial Information Authority of Japan (GSI), and the GEBCO_08 Grid of the General Bathymetric Chart of the Oceans (GEBCO). Finally, the authors are grateful to the anonymous reviewers and guest editor, whose comments have improved this paper.

Author contributions

SS conceived the research project. SS and MN collected the samples. HI and TD acquired and processed the fission-track and U–Pb data with support from TH. MN performed microscopic observations of the hydrothermal minerals. MKn and BK acquired and processed the (U–Th)/He data. MKw acquired and processed the fluid-inclusion analyses data. TY and SK acquired and processed the additional U–Pb data. YO acquired and processed the EPMA data. SS wrote the manuscript with input from all co-authors.

Funding

This study was funded by the Ministry of Economy, Trade and Industry (METI), Japan as part of its R&D supporting program entitled "Establishment of Advanced Technology for Evaluating the Long-term Geosphere Stability on Geological Disposal Project of Radioactive Waste (Fiscal Years 2018–2021), Grant Number JPJ007597". The University of Melbourne thermochronology laboratory receives support under the AuScope program of the National Collaborative Research Infrastructure Strategy (NCRIS).

Availability of data and materials

The data for this paper are presented in the tables and additional information.

Declarations

Ethics approval and consent to participate

Not applicable.

Consent for publication

Not applicable.

Competing interests

The authors declare that they have no competing interests.

Author details

[1]Tono Geoscience Center, Japan Atomic Energy Agency, Toki 509-5102, Japan. [2]Kyoto Fission-Track Co., Ltd., Kyoto 603-8832, Japan. [3]School of Geography, Earth and Atmospheric Sciences, University of Melbourne, Victoria 3010, Australia. [4]Geochemical Research Center, Graduate School of Science, The University of Tokyo, Tokyo 113-0033, Japan.

Received: 9 July 2023 Accepted: 18 October 2023
Published online: 28 November 2023

References

Ahnert F (1970) Functional relationships between denudation, relief, and uplift in large mid-latitude drainage basins. Am J Sci 268:243–263

Aramaki S (1965) Mode of emplacement of acid igneous complex (Kumano Acidic Rocks) in Southeastern Kii peninsula. J Geol Soc Japan 71:525–540

Arne DC, Green PF, Duddy IR (1990) Thermochronologic constraints on the timing of Mississippi Valley-type ore formation from apatite fission track analysis. Int J Radiat Appl Instrum Part D Nucl Tracks Radiat Meas 17:319–323

Arnulf AF, Bassett D, Harding AJ, Kodaira S, Nakanishi A, Moore G (2022) Upper-plate controls on subduction zone geometry, hydration and earthquake behaviour. Nat Geosci 15:143–148
Ault AK, Frenzel M, Reiners PW, Woodcock NH, Thomson SN (2016) Record of paleofluid circulation in faults revealed by hematite (U-Th)/He and apatite fission-track dating: an example from Gower Peninsula fault fissures, Wales. Lithosphere 8:379–385
Ault AK, Gautheron C, King GE (2019) Innovations in (U–Th)/He, fission track, and trapped charge thermochronometry with applications to earthquakes, weathering, surface-mantle connections, and the growth and decay of mountains. Tectonics. https://doi.org/10.1029/2018TC005312
Awan MA, Kimura K (1996) Thermal structure and uplift of the Cretaceous Shimanto Belt, Kii Peninsula, Southwest Japan: an illite crystallinity and illite b_0 lattice spacing study. The Island Arc 5:69–88
Beinlich A, John T, Vrijmoed JC, Tominaga M, Magna T, Podladchikov YY (2020) Instantaneous rock transformations in the deep crust driven by reactive fluid flow. Nat Geosci 13:307–311
Bowen R (2011) Geothermal resources, 2nd edn. Springer
Carlson WD, Donelick RA, Ketcham RA (1999) Variability of apatite fission-track annealing kinetics: I. Experimental Results. Am Mineral 84:1213–1223
Cherniak DJ, Watson EB (2000) Pb diffusion in zircon. Chem Geol 172:5–24
Committee for Catalog of Quaternary Volcanoes in Japan (1999) Catalog of Quaternary Volcanoes in Japan v1.0, CD-ROM Version, Volcanological Society of Japan
Coutts DS, Matthews WA, Hubbard SM (2019) Assessment of widely used methods to derive depositional ages from detrital zircon populations. Geosci Front 10:1421–1435
Cox SF (2005) Coupling between deformation, fluid pressures, and fluid flow in ore-producing hydrothermal systems at depth in the crust, Economic Geology 100th Anniversary Volume, pp.39–75
d'Alessio MA, Blythe AE, Bürgmann R (2003) No frictional heat along the San Gabriel fault, California: evidence from fission-track thermochronology. Geology 31:541–544
Danišík M, McInnes BI, Kirkland CL, McDonald BJ, Evans NJ, Becker T (2017) Seeing is believing: visualization of He distribution in zircon and implications for thermal history reconstruction on single crystals. Sci Adv 3:e1601121
Dickinson WR, Gehrels GE (2009) Use of U-Pb ages of detrital zircons to infer maximum depositional ages of strata: a test against a Colorado Plateau Mesozoic database. Earth Planet Sci Lett 288:115–125
Donelick RA, Miller DS (1991) Enhanced TINT fission track densities in low spontaneous track density apatite using ^{252}Cf-derived fission fragment tracks: a model and experimental observations. Nucl Tracks Radiat Meas 18:301–307
Farley KA (2000) Helium diffusion from apatite' General behavior as illustrated by Durango fluorapatite. J Geophys Res 105:2903–2914
Farley KA, Wolf RA, Silver LT (1996) The effects of long alpha-stopping distances on (U-Th)/He ages. Geochim Cosmochim Acta 60:4223–4229
Flowers RM, Ketcham RA, Shuster DL, Farley KA (2009) Apatite (U–Th)/He thermochronometry using a radiation damage accumulation and annealing model. Geochim Cosmochim Acta 73:2347–2365
Fuji-ta K, Ogawa Y, Yamaguchi S, Yakawa K (1997) Magnetotelluric imaging of the SW Japan forearc a lost paleoland revealed? Phys Earth Planet Inter 102:231–238
Galbraith RF (1990) The radial plot: graphical assessment of spread in ages. Int J Radiat Appl Instrum Part D Nucl Tracks Radiat Meas 17:207–214
Galbraith RF, Green PF (1990) Estimating the component ages in a finite mixture. Int J Radiat Appl Instrum Part D Nucl Tracks Radiat Meas 17:197–206
Gleadow AJW, Duddy IR, Green PF, Lovering JF (1986) Confined fission track lengths in apatite: a diagnostic tool for thermal history analysis. Contrib Miner Petrol 94:405–415
Gleadow AJW, Harrison M, Kohn B, Lugo-Zazueta R, Phillips D (2015) The Fish Canyon Tuff: anew look at an old low-temperature thermochronology standard. Earth Planet Sci Lett 424:95–108
Guenthner WR, Reiners PW, Ketcham RA, Nasdala L, Giester G (2013) Helium diffusion in natural zircon: radiation damage, anisotropy, and the interpretation of zircon (U-Th)/He thermochronology. Am J Sci 313:145–198
Hanamuro T, Umeda K, Takashima I, Negishi Y (2008) Thermal history of the alteration zones around hot springs at Hongu and Totsukawa area Southern Kii Peninsula, Southwest Japan. Jpn Magazine Mineral Petrol Sci 37:27–38
Hasebe N, Tagami T (2001) Exhumation of an accretionary prism: results from fission track thermochronology of the Shimanto Belt, southwest Japan. Tectonophysics 331:247–267
Hasebe N, Watanabe H (2004) Heat influx and exhumation of the Shimanto accretionary complex: miocene fission track ages from the Kii Peninsula, southwest Japan. Island Arc 13:533–543
Hasebe N, Tagami T, Nishimura S (1993a) The evidence of along-arc differential uplift of the Shimanto accretionary complex: fission track thermochronology of the Kumano Acidic Rocks, Southwest Japan. Tectonophysics 224:327–335
Hasebe N, Tagami T, Nishimura S (1993b) Evolution of the Shimanto accretionary complex: a fission-track thermochronologic study. Geol Soc Am Spec Pap 273:121–136
Hasebe N, Tagami T, Nishimura S (1994) Towards zircon fission-track thermochronology: reference framework for confined track length measurements. Chem Geol (isotope Geoscience Section) 112:169–178
Hasebe N, Tagami T, Nishimura S (1997) Melange-forming processes in the development of an accretionary prism: evidence from fission track thermochronology. J Geophys Res 102:7659–7672
Hasebe N, Suwargadi BW, Nishimura S (2000) Fission track ages of the Omine Acidic Rocks, Kii Peninsula, Southwest Japan. Geochem J 34:229–235
Hirose F, Nakajima J, Hasegawa A (2008a) Three-dimensional seismic velocity structure and configuration of the Philippine Sea slab in southwestern Japan estimated by double-difference tomography. J Geophys Res 113:B09315. https://doi.org/10.1029/2007JB005274
Hirose F, Nakajima J, Hasegawa A (2008b) Three-dimensional velocity structure and configuration of the Philippine Sea slab beneath Kanto district, central Japan, estimated by double-difference tomography, Zisin (Journal of the Seismological Society of Japan. 2nd ser.), 60:123–138
Hoshi H (2018) Miocene clockwise rotation of Southwest Japan. J Geol Soc Jpn 124:675–691
Hoshi H, Kato D, Ando Y, Nakashima K (2015) Timing of clockwise rotation of Southwest Japan: constraints from new middle Miocene paleomagnetic results. Earth Planets Space 67:92. https://doi.org/10.1186/s40623-015-0266-3
Hoshi H, Kawakami Y, Iwano H, Danhara T (2022) Zircon U-Pb and fission-track ages of felsic tuff from the Ryujin Complex in the Shimanto Accretionary Prism on the eastern part of the Kii Peninsula, Japan. J Geol Soc Japan 128:229–237
Hourigan JK, Reiners PW, Brandon MT (2005) U-Th zonation dependent alpha-ejection in (U-Th)/He chronometry. Geochim Cosmochim Acta 69:3349–3365
Iwano H, Danhara T, Hoshi H, Kawakami Y, Sumii T, Shinjoe H, Wada Y (2007) Simultaneity and similarity of the Muro Pyroclastic Flow Deposit and the Kumano Acidic Rocks in Kii Peninsula, southwest Japan, based on fission track ages and morphological characteristics of zircon. J Geol Soc Japan 113:326–339
Iwano H, Danhara T, Hoshi H (2009) Fission track ages on apatite from Miocene igneous rocks in the Kii Peninsula, Japan. J Geol Soc Japan 115:427–432
Iwano H, Orihashi Y, Hirata T, Ogasawara M, Danhara T, Horie K, Hasebe N, Sueoka S, Tamura A, Hayasaka Y, Katsube A, Ito H, Tani K, Kimura J, Chang Q, Kouchi Y, Haruta Y, Yamamoto K (2013) An inter-laboratory evaluation of OD-3 zircon for use as a secondary U-Pb dating standard. Island Arc 22:382–394
Jess S, Enkelmann E, Grasby SE, Fraser K (2021) Determining the lifespan of hydrothermal systems using thermochronology and thermal modeling. J Geophys Res Earth Surface. https://doi.org/10.1029/2021JF006286
Kato A, Saiga A, Takeda T, Iwasaki T, Matsuzawa T (2014) Non-volcanic seismic swarm and fluid transportation driven by subduction of the Philippine Sea slab beneath the Kii Peninsula, Japan, Earth, Planets and Space, 66:86, http://www.earth-planets-space.com/content/66/1/86
Kawakami Y, Hoshi H, Yamaguchi Y (2007) Mechanism of caldera collapse and resurgence: observations from the northern part of the Kumano Acidic Rocks Kii Peninsula, Southwest Japan. J Volcanol Geothermal Res 167:263–281
Kawasaki M (1980) Omine Acid Rocks, Kii Peninsula: geology and major element chemistry. J Jpn Assoc Mineral Petrol Econ Geol 75:86–102

Kazahaya K, Takahashi M, Yasuhara M, Nishio Y, Inamura A, Morikawa N, Sato T, Takahashi HA, Kitaoka K, Ohsawa S, Oyama Y, Ohwada M, Tsukamoto H, Horiguchi K, Tosaki Y, Kirita T (2014) Spatial distribution and feature of slab-related deep-seated fluid in SW Japan. J Jpn Assoc Hydrol Sci 44:3–16
Ketcham RA (2005) Forward and inverse modeling of low-temperature thermochronometry data. Rev Mineral Geochem 58:275–314
Ketcham RA (2019) Fission-track annealing: From geologic observations to thermal history modeling, In Malusà MG, Fitzgerald PG (eds.) Fission-Track Thermochronology and its Application to Geology, Springer Textbooks in Earth Sciences, Geography and Environment, pp.49–75
Ketcham RA, Donelick RA, Carlson WD (1999) Variability of apatite fission-track annealing kinetics: III. Extrapolation to geological time scales. Am Mineral 84:1235–1255
Ketcham RA, Carter A, Donelick RA, Barbarand J, Hurford AJ (2007) Improved modeling of fission-track annealing in apatite. Am Miner 92:799–810
Kimbara K (2005) Distribution Map and Catalogue of Hot and Mineral Springs in Japan (Second Edition) (CD-ROM Version), Geological Survey of Japan, AIST, Tsukuba
Kimura J, Stern RJ, Yoshida T (2005) Reinitiation of subduction and magmatic responses in SW Japan during Neogene time. Geol Soc Am Bull 117:969–986
Kodaira S, Hori T, Ito A, Miura S, Fujie G, Park J-O, Baba T, Sakaguchi H, Kaneda Y (2006) A cause of rupture segmentation and synchronization in the Nankai trough revealed by seismic imaging and numerical simulation. J Geophys Res 111:B09301. https://doi.org/10.1029/2005JB004030
Louis S, Luijendijk E, Dunkl I, Person M (2019) Episodic fluid flow in an active fault. Geology 47:938–942
Malusà MG, Fitzgerald PG (2020) The geologic interpretation of the detrital thermochronology record within a stratigraphic framework, with examples from the European Alps, Taiwan and the Himalayas. Earth Sci Rev 201:103074. https://doi.org/10.1016/j.earscirev.2019.103074
Malusà MG, Fitzgerald PG (2019a) Fission-track thermochronology and its application to geology, Springer Textbooks in Earth Sciences, Geography and Environment
Malusà MG, Fitzgerald PG (2019b) From cooling to exhumation: setting the reference frame for the interpretation of thermochronologic data, In Malusà MG, Fitzgerald PG (eds.) Fission-Track Thermochronology and its Application to Geology, Springer Textbooks in Earth Sciences, Geography and Environment, pp.49–75
Márton I, Morits R, Spikings R (2010) Application of low-temperature thermochronology to hydrothermal ore deposits: formation, preservation and exhumation of epithermal gold systems from the Eastern Rhodopes, Bulgaria. Tectonophysics 483:240–254
Matsumoto T, Kawabata T, Matsuda J-I, Yamamoto K (2003) $^{3}He/^{4}He$ ratios in well gases in the Kinki district, SW Japan: surface appearance of slab-derived fluids in a non-volcanic area in Kii Peninsula. Earth Planet Sci Lett 216:221–230
Matsuzaki T, Kakuta C, Ishimaru T, Kamata H, Danhara T, Iwano H, Yoshioka T (2004) Evaluation of thermal effects of large-scale pyroclastic flow deposits on basement rocks by fission-track method. J Jpn Soc Eng Geol 45:238–248
Meissner R, Wever Th (1992) The possible role of fluids for the structuring of the continental crust. Earth Sci Rev 32:19–32
Milesi G, Soliva R, Monié P, Münch P, Bellanger M, Bruguier O, Bonno M, Taillefer A, Mayolle S (2019) Mapping a geothermal anomaly using apatite (U-Th)/He thermochronology in the Têt fault damage zone, eastern Pyrenees, France. Terra Nova 31:569–576
Milesi G, Monié P, Münch P, Soliva R, Taillefer A, Bruguier O, Bellanger M, Bonno M, Martin C (2020) Tracking geothermal anomalies along a crustal fault using (U–Th)/He apatite thermochronology and rare-earth element (REE) analyses: the example of the Têt fault (Pyrenees, France). Solid Earth 11:1747–1771
Misra KC (2000) Formation of mineral deposits, In: Understanding Mineral Deposits. Springer, Dordrecht. https://doi.org/10.1007/978-94-011-3925-0_2
Mitchell SG, Reiners PW (2003) Influence of wildfires on apatite and zircon (U-Th)/He ages. Geology 31:1025–1028
Miura D (1999) Arcuate pyroclastic conduits, ring faults, and coherent floor at Kumano caldera, southwest Honshu Japan. J Volcanol Geothermal Res 92:271–294
Morikawa N, Kazahaya K, Takahashi M, Inamura A, Takahashi H, Yasuhara M, Ohwada M, Sato T, Nakama A, Handa H, Sumino H, Nagao K (2016) Widespread distribution of ascending fluids transporting mantle helium in the fore-arc region and their upwelling processes: Noble gas and major element composition of deep groundwater in the Kii Peninsula, southwest Japan. Geochemica Et Cosmochimica Acta 182:173–196
Mukuhira Y, Uno M, Yoshida K (2022) Slab-derived fluid storage in the crust elucidated by earthquake swarm. Commun Earth Environ 3:286. https://doi.org/10.1038/s43247-022-00610-7
Murakami M, Tagami T (2004) Dating pseudotachylyte of the Nojima fault using the zircon fission-track method. Geophys Res Lett 31:L12604. https://doi.org/10.1029/2004GL020211
Murakami M, Tagami T, Hasebe N (2002) Ancient thermal anomaly of an active fault system: Zircon fission-track evidence from Nojima GSJ 750 m borehole samples. Geophys Res Lett 29:2123. https://doi.org/10.1029/2002GL015679
Murray KE, Braun J, Reiners PW (2018) Toward robust interpretation of low-temperature thermochronometers in magmatic terranes. Geochem Geophys Geosyst 19:3739–3763. https://doi.org/10.1029/2018GC007595
Nakajima J (2023) The Wakayama earthquake swarm in Japan. Earth Planets Space 75:48. https://doi.org/10.1186/s40623-023-01807-6
Nakajima J, Hasegawa A (2007) Subduction of the Philippine Sea plate beneath southwestern Japan: slab geometry and its relationship to arc magmatism. J Geophys Res 112:B08306. https://doi.org/10.1029/2006JB004770
Nakajima J, Hirose F, Hasegawa A (2009) Seismotectonics beneath the Tokyo metropolitan area, Japan: Effect of slab-slab contact and overlap on seismicity. J Geophys Res 114:B08309. https://doi.org/10.1029/2008JB006101
Nakata T, Imaizumi T (2002) Digital active fault map of Japan. University of Tokyo Press, Tokyo
National Institute of Advanced Industrial Science and Technology (2016) https://www.nsr.go.jp/data/000186554.pdf
National Institute of Advanced Industrial Science and Technology (2017) https://www.nsr.go.jp/data/000210763.pdf
Obara K (2002) Nonvolcanic deep tremor associated with subduction in southwest Japan. Science 296:1679–1681
Ohira H, Kasai M, Yamamoto D, Takasu A (2016) Fission track ages from accretionary complexes of Cretaceous Shimanto Belt in the Kii Peninsula, SW Japan. Geosci Rep Shimane Univ 34:69–75
Ohmori H (1978) Relief structure of the Japanese mountains and their stages in geomorphic development. Bull Dep Geogr 10:31–85
Orihashi Y, Iwano H, Hirata T, Danhara T, Shinjoe H (2007) U-Pb ages and trace element compositions of reddish, colorless, and detrital zircons in the Kumano Acidic Rocks in the Outer Zone of southwest Japan and origin of the host magma. J Geol Soc Japan 113:366–383
Reiners PW (2009) Nonmonotonic thermal histories and contrasting kinetics of multiple thermochronometers. Geochim Cosmochim Acta 73:3612–3629
Reiners PW, Spell TL, Nicolescu S, Zanetti KA (2004) Zircon (U-Th)/He thermochronometry: He diffusion and comparisons with $^{40}Ar/^{39}Ar$ dating. Geochim Cosmochim Acta 68:1857–1887
Reiners PW, Ehlers TA, Zeitler PK (2005) Past, present, and future of thermochronology. Rev Mineral Geochem 58:1–18
Reiners PW, Thomson SN, McPhillips D, Donelick RA, Roering JJ (2007) Wildfire thermochronology and the fate and transport of apatite in hillslope and fluvial environments. J Geophys Res 112:F04001. https://doi.org/10.1029/2007JF000759
Roedder E (1984) Fluid inclusions. Mineralogical Society of America, Chantilly
Sato T, Yamato Omine Research Group (2006) Omine and Odai Cauldrons: arcuate and semicircular faults, dike swarms and collapse structure in the central area of the Kii Mountains, Southwest Japan. Earth Sci (chikyu Kagaku) 60:403–413
Shuster DL, Flowers RM, Farley KA (2006) The influence of natural radiation damage on helium diffusion kinetics in apatite. Earth Planet Sci Lett 249:148–161

Sibson RH, Rowland JV (2003) Stress, fluid pressure and structural permeability in seismogenic crust, North Island, New Zealand. Geophys J Int 154:584–594
Sueoka S, Tagami T (2019) Low-temperature thermochronological database of bedrock in the Japanese Islands. Island Arc 28:e12305. https://doi.org/10.1111/iar.12305
Sueoka S, Tsutsumi H, Tagami T (2016) New approach to resolve the amount of Quaternary uplift and associated denudation of the mountain ranges in the Japanese Islands. Geosci Front 7:197–210
Sueoka S, Ikuho Z, Hasebe N, Murakami M, Yamada R, Tamura A, Arai S, Tagami T (2019) Thermal fluid activities along the Mozumi-Sukenobu fault, central Japan, identified via zircon fission-track thermochronometry. J Asian Earth Sci X 2:100011
Sumii T, Shinjoe H (2003) K-Ar ages of the Ohmine Granitic Rocks, south-west Japan. Island Arc 12:335–347
Sumii T, Uchiumi S, Shinjoe H, Shimoda G (1998) Re-examination on K-Ar age of the Kumano Acidic Rocks in Kii Peninsula, Southwest Japan. J Geol Soc Japan 104:387–394
Suzuki H (1993) Discovery of Eocene radiolaria from the Otonashigawa Belt of the Shimanto Superbelt in the Kii Peninsula, Southwest Japan. Earth Sci (chikyu Kagaku) 47:75–79
Tagami T (2019) Application of fission-track thermochronology to understand fault zones, In Malusà MG, & Fitzgerald PG (eds.) Fission-Track Thermochronology and its Application to Geology, Springer Textbooks in Earth Sciences, Geography and Environment, pp.221–233
Tagami T, Murakami M (2007) Probing fault zone heterogeneity on the Nojima fault: constraints from zircon fission-track analysis of borehole samples. Tectonophysics 443:139–152
Tagami T, Shimada C (1996) Natural long-term annealing of the zircon fission track system around a granitic pluton. J Geophys Res 101:8245–8255
Tagami T, Hasebe N, Shimada C (1995) Episodic exhumation of accretionary complexes: fission-track thermochronologic evidence from the Shimanto Belt and its vicinities, southwest Japan. Island Arc 4:209–230
Tagami T, Hasebe N, Kamohara H, Takemura K (2001) Thermal anomaly around the Nojima Fault as detected by fission-track analysis of Ogura 500 m borehole samples. The Island Arc 10:457–464
Tamburello G, Chiodini G, Ciotoli G, Procesi M, Rouwet D, Sandri L, Carbonara N, Masciantonio C (2022) Global thermal spring distribution and relationship to endogenous and exogenous factors. Nat Commun 13:6378
Tanaka H, Ito T, Nohara T, Ando M (2007) Descriptions of meso- and microscopic structures of fault zone rocks obtained from tunnel penetrated across the Mozumi-Sukenobu fault, central Japan, In Ando, M. (eds.) Geodynamics of Atotsugawa Fault System, Terrapub, pp.103–121
Tokiwa T, Takeuchi M, Shimura Y, Ota A, Yamamoto K (2016) U-Pb ages of detrital zircon from the tuffaceous sandstone of the Shimanto Belt in the Kii Peninsula. J Geol Soc Japan 122:625–635
Tokuoka T, Harata T, Inouchi Y, Ishigami T, Kimura K, Kumon F, Nakajo K, Nakaya S, Sakamoto T, Suzuki H, Taniguchi J (1981) Geology of the Ryujin district. Quadrangle Series, scale 1:50,000, 69p, Geological Survey of Japan, Tsukuba (in Japanese with English abstract)
Umeda K, Ogawa Y, Asamori K, Negi T (2006) Aqueous fluids derived from a subducting slab: observed high ^{3}He emanation and conductive anomaly in a non-volcanic region, Kii Peninsula southwest Japan. J Volcanol Geoth Res 149:47–61
Umeda K, Hanamuro T, Yamada K, Negishi Y, Iwano H, Danhara T (2007) Thermochronology of non-volcanic hydrothermal activity in the Kii Peninsula, Southwest Japan: evidence from fission track dating and helium isotopes in paleo-hydrothermal fluids. Radiat Meas 42:1647–1654
Underwood MB, Laughland MM, Kang SM (1993) A comparison among organic and inorganic indicators of diagenesis and low-temperature metamorphism, Tertiary Shimanto Belt, Shikoku, Japan, In Underwood, M. B. (ed.) Thermal Evolution of the Tertiary Shimanto Belt, Southwest Japan: An Example of Ridge-Trench Interaction, Geological Society of America, Special Paper, 273, pp.49–75
Vermeesch P (2018) IsoplotR: a free and open toolbox for geochronology. Geosci Front 9:1479–1493
Wakita K, Igawa T, Takarada S (2009) Seamless geological map of Japan at a scale of 1:200,000 DVD edition, Digital Geoscience Map DGM G-16, Geological Society of Japan, AIST, Tsukuba
Wang C, Deng J, Santosh M, Carranza EJM, Gong Q, Guo C, Xia R, Lai X (2015) Timing, tectonic implications and genesis of gold mineralization in the Xincheng gold deposit, China: C-H–O isotopes, pyrite Rb–Sr and zircon fission track thermochronometry. Ore Geol Rev 65:659–673
Wessel P, Smith WHF (1991) Free software helps map and display data. Eos Trans Am Geophys Union 72:441
Wilson NSF, Zentilli M, Reynolds PH, Boric R (2003) Age of mineralization by basinal fluids at the El Soldado manto-type copper deposit, Chile: ^{40}Ar/^{39}Ar geochronology of K-feldspar. Chem Geol 197:161–176
Wölfler A, Kurz W, Danišík M, Rabitsch R (2010) Dating of fault zone activity by apatite fission track and apatite (U–Th)/He thermochronometry: a case study from the Lavanttal fault system (Eastern Alps). Terra Nova 22:274–282
Yamada R, Tagami T, Nishimura S (1995) Confined fission-track length measurement of zircon: assessment of factors affecting the paleotemperature estimate. Chem Geol (isotope Geoscience Section) 119:293–306
Yamada R, Murakami M, Tagami T (2007) Statistical modelling of annealing kinetics of fission tracks in zircon; reassessment of laboratory experiments. Chem Geol 236:75–91
Yamaguchi S, Uyeshima M, Murakami H, Sutoh S, Tanigawa D, Ogawa T, Oshiman N, Yoshimura R, Aizawa K, Shiozaki I, Kasaya T (2009) Modification of the Network-MT method and its first application in imaging the deep conductivity structure beneath the Kii Peninsula, southwestern Japan. Earth Planets Space 61:957–971
Yamaji A, Yoshida T (1998) Multiple tectonic events in the Miocene Japan arc: the Heike microplate hypothesis. J Mineral Petrol Econ Geol 93:389–408
Yonekura, N., Kaizuka, S., Nogami, M., Chinzei, K. (eds.) (2001) Regional Geomorphology of the Japanese Islands, vol. 1, Introduction to Japanese Geomorphology, University of Tokyo Press, Tokyo, 349p
Yuan W, Qiugen Z, Bao Z, Dong J, Carter A, An Y (2009) Zircon fission track thermochronology constraints on mineralization epochs in Altai Mountains, northern Xinjiang, China. Radiat Meas 44:950–954
Zhao D, Kanamori H, Negishi H, Wiens D (1996) Tomography of the source area of the 1995 Kobe earthquake: Evidence for fluids at the hypocenter? Science 274:1891–1894

Publisher's Note